Article

Cell

Vitamin A-Retinoic Acid Signaling Regulates Hematopoietic Stem Cell Dormancy

Graphical Abstract

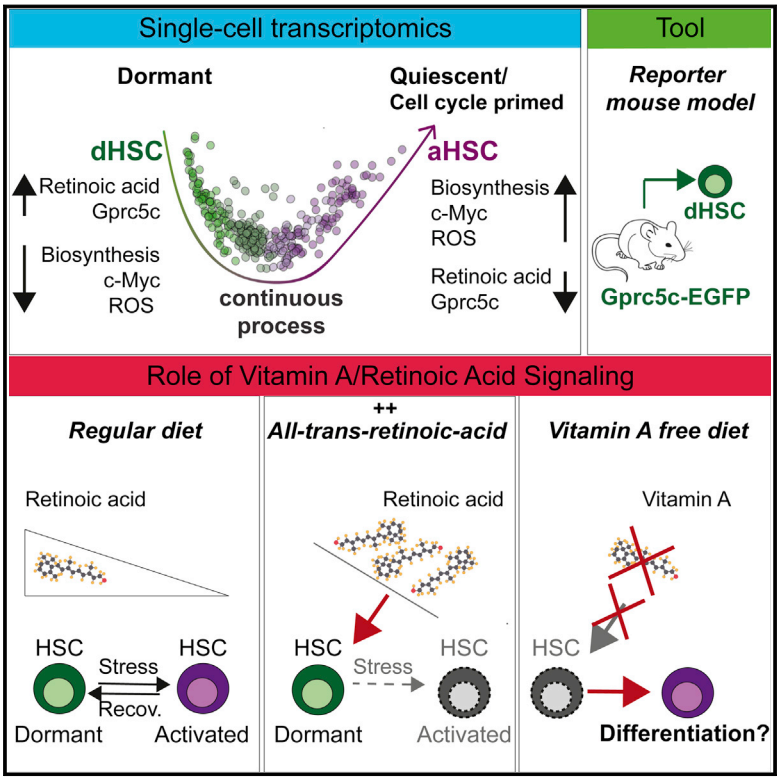

Highlights

- Continuous increase of biosynthesis during transition from dormant to active HSCs
- Gprc5c-EGFP reporter mice allow identification and isolation of dormant HSCs
- Retinoic acid-vitamin A regulates HSC plasticity during stress-mediated activation
- Vitamin A-deficient diet impairs the HSC compartment in mice

Authors

Nina Cabezas-Wallscheid, Florian Buettner, Pia Sommerkamp, ..., Michael A. Rieger, Oliver Stegle, Andreas Trumpp

Correspondence

n.cabezas@dkfz.de (N.C.-W.), a.trumpp@dkfz.de (A.T.)

In Brief

Metabolic inputs control the entry and exit of hematopoietic stem cells from dormancy and suggest the potential application of vitamin A in hematopoietic disorders and leukemias.

Cabezas-Wallscheid et al., 2017, Cell *169*, 807–823
May 18, 2017
http://dx.doi.org/10.1016/j.cell.2017.04.018

CellPress

Cell

Vitamin A-Retinoic Acid Signaling Regulates Hematopoietic Stem Cell Dormancy

Nina Cabezas-Wallscheid,[1,2,12,*] Florian Buettner,[3,12] Pia Sommerkamp,[1,2] Daniel Klimmeck,[1,2] Luisa Ladel,[1,2] Frederic B. Thalheimer,[4] Daniel Pastor-Flores,[5] Leticia P. Roma,[5] Simon Renders,[1,2] Petra Zeisberger,[1,2] Adriana Przybylla,[1,2] Katharina Schönberger,[1,2] Roberta Scognamiglio,[1,2] Sandro Altamura,[6] Carolina M. Florian,[7] Malak Fawaz,[4] Dominik Vonficht,[1,2] Melania Tesio,[1,2] Paul Collier,[8] Dinko Pavlinic,[8] Hartmut Geiger,[7] Timm Schroeder,[9] Vladimir Benes,[8] Tobias P. Dick,[5] Michael A. Rieger,[4] Oliver Stegle,[3,11] and Andreas Trumpp[1,2,10,11,13,*]

[1]Division of Stem Cells and Cancer, German Cancer Research Center (DKFZ) and DKFZ-ZMBH Alliance, 69120 Heidelberg, Germany
[2]Heidelberg Institute for Stem Cell Technology and Experimental Medicine (HI-STEM gGmbH), 69120 Heidelberg, Germany
[3]European Molecular Biology Laboratory, European Bioinformatics Institute (EBI), Wellcome Genome Campus, Hinxton, Cambridge CB10 1SD, UK
[4]LOEWE Center for Cell and Gene Therapy and Department of Medicine, Hematology/Oncology, Goethe University Frankfurt, 60590 Frankfurt am Main, Germany
[5]Division of Redox Regulation, DKFZ-ZMBH Alliance, German Cancer Research Center (DKFZ), 69120 Heidelberg, Germany
[6]Department of Pediatric Hematology, Oncology and Immunology, University of Heidelberg, 69120 Heidelberg, Germany
[7]Institute for Molecular Medicine, Stem Cells and Aging, Ulm University, 89081 Ulm, Germany
[8]Genomics Core Facility, European Molecular Biology Laboratory (EMBL), 69117 Heidelberg, Germany
[9]Department of Biosystems Science and Engineering (D-BSSE), ETH Zurich, 4058 Basel, Switzerland
[10]German Cancer Consortium (DKTK), 69120 Heidelberg, Germany
[11]Senior author
[12]These authors contributed equally
[13]Lead Contact
*Correspondence: n.cabezas@dkfz.de (N.C.-W.), a.trumpp@dkfz.de (A.T.)
http://dx.doi.org/10.1016/j.cell.2017.04.018

SUMMARY

Dormant hematopoietic stem cells (dHSCs) are atop the hematopoietic hierarchy. The molecular identity of dHSCs and the mechanisms regulating their maintenance or exit from dormancy remain uncertain. Here, we use single-cell RNA sequencing (RNA-seq) analysis to show that the transition from dormancy toward cell-cycle entry is a continuous developmental path associated with upregulation of biosynthetic processes rather than a stepwise progression. In addition, low Myc levels and high expression of a retinoic acid program are characteristic for dHSCs. To follow the behavior of dHSCs in situ, a *Gprc5c*-controlled reporter mouse was established. Treatment with all-*trans* retinoic acid antagonizes stress-induced activation of dHSCs by restricting protein translation and levels of reactive oxygen species (ROS) and Myc. Mice maintained on a vitamin A-free diet lose HSCs and show a disrupted re-entry into dormancy after exposure to inflammatory stress stimuli. Our results highlight the impact of dietary vitamin A on the regulation of cell-cycle-mediated stem cell plasticity.

INTRODUCTION

Hematopoietic stem cells (HSCs) are unique in their capacity to self-renew and replenish the entire blood system upon transplantation in a serial manner (Seita and Weissman, 2010; Till and McCulloch, 1961). HSCs give rise to a pool of multipotent progenitors (MPPs), which generate lineage-restricted progenitors, and finally, mature effector cells (Graf and Enver, 2009). We and others have recently identified a sub-population of HSCs by long-term label-retaining cell (LRC) assays, which are characterized by an extremely low in vivo proliferation history with only approximately five cell divisions per lifetime in a healthy mouse as shown by mathematical modeling (van der Wath et al., 2009; Wilson et al., 2008). These so-called dormant HSCs (dHSCs), (Lineage$^-$, Sca-1$^+$, c-Kit$^+$, [LSK], CD150$^+$, CD48$^-$, CD135$^-$, CD34$^-$, LRC$^+$), represent only ~20%–30% of all HSCs (~700 cells out of 100 million hematopoietic cells in the murine bone marrow) but harbor the highest long-term reconstitution potential (summarized in Figure 1A) (Bernitz et al., 2016; Qiu et al., 2014; Takizawa et al., 2011; Wilson et al., 2008). dHSCs are reversibly activated in response to stress signals such as interferons, lipopolysaccharide (LPS), or chemotherapy and are of critical importance in the repair processes activated in response to bacterial/viral infections or after severe bleeding (Baldridge et al., 2010; Essers et al., 2009; Walter et al., 2015). dHSCs progress to active HSCs (aHSCs), which comprise ~70%–80% of the HSC pool, are slowly dividing, and harbor a reduced reconstitution potential (Wilson et al., 2008). To date, the molecular fingerprint of HSC dormancy at the population and single-cell level, as well as the mechanism controlling their reversible cycle between dormant and active states during homeostasis and stress, remains largely unresolved. We have recently reported that retinoic acid (RA) metabolism is molecularly enriched in HSCs compared to downstream multipotent progenitor populations (Cabezas-Wallscheid et al., 2014). RA

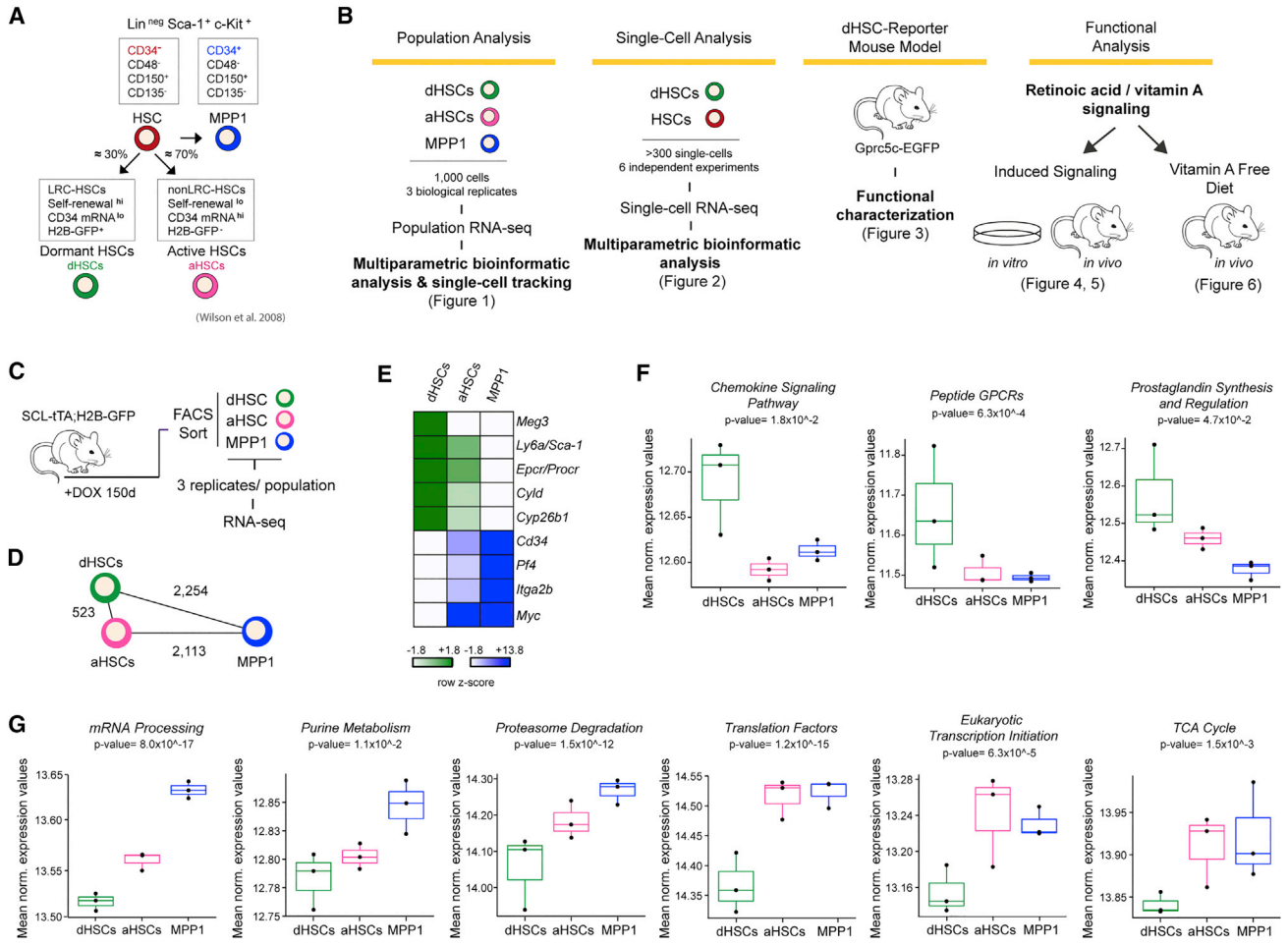

Figure 1. Analysis of the Dormant Hematopoietic Stem Cell Compartment

(A) The dHSC compartment. Main findings summarized in Wilson et al. (2008).

(B) Experimental study design.

(C) RNA-seq workflow.

(D) Closest neighbor analysis. Relative transcriptome distances of dHSCs, aHSCs, and MPP1 based on the numbers of differentially expressed genes in pairwise comparisons (FDR <0.1).

(E) RNA-seq expression from dHSCs to MPP1. Heatmap showing average *Z* scores of RNA-seq normalized expression values across replicates for selected marker genes.

(F and G) Signaling pathway enrichment analysis within dHSCs, aHSCs, and MPP1. Signaling pathways enriched (F) and depleted (G) expressed in dHSCs compared to aHSCs and MPP1. Shown are mean expression levels of enriched gene sets for three replicates (FDR <0.1).

See also Figure S1 and Table S1.

signaling has been shown to affect embryonic hematopoiesis and leukemogenesis (Chanda et al., 2013; Collins, 2008). However, its role in hematopoietic stem/progenitor biology remains controversial (Chute et al., 2006; Ghiaur et al., 2013; Purton et al., 1999, 2000). RA is produced by two sequential oxidation steps from dietary vitamin A (Tang and Gudas, 2011). Vitamin A is an essential nutrient required for the normal function of the visual system, growth and development, and maintenance of epithelial cellular integrity, immune function, and reproduction (Brown and Noelle, 2015; Mora et al., 2008). Lack of vitamin A is common in pre-school children, associated with night blindness as well as in skin and immune system deficiencies (Brown and Noelle, 2015; Mora et al., 2008; Wagner, 1940). Although the consequences of a vitamin A-free diet have been extensively studied in the context of the immune system (Brown and Noelle, 2015; Mora et al., 2008), the specific relevance of vitamin A for the maintenance and function of HSCs is unresolved.

RESULTS

Whole-Transcriptome Analysis of Dormant HSCs

To establish a global molecular dormancy signature, we performed whole-transcriptome (RNA sequencing [RNA-seq]) analysis of dHSCs (LRCs), aHSCs (non-LRCs), and multipotent progenitors 1 (MPP1; Figures 1A–1C, S1A, and S1B). Briefly, we used fluorescence-activated cell sorting (FACS)-sorted dHSCs,

aHSCs, and MPP1 from SCL-tTA;H2B-GFP mice (hereafter termed SCL) chased for 150 days with doxycycline (DOX) (Figure S1A) (Wilson et al., 2008) and generated RNA-seq data as previously described (Figure S1B) (Cabezas-Wallscheid et al., 2014; Klimmeck et al., 2014). We identified a set of 27,236 expressed genes including protein-coding genes, pseudogenes, and long non-coding RNAs (Figure S1C; Table S1). Principle component analysis (PCA) showed a closer relationship between dHSCs and aHSCs compared to either one to MPP1 (Figure S1D). Consistently, we observed a large number of differentially expressed genes between MPP1 and either of the two HSC populations (false discovery rate [FDR] <0.1; Figure 1D). These results indicate that the transcriptomes of dHSCs and aHSCs are more similar to each other than to MPP1.

Dormant HSCs Exhibit Low Expression of Essential Biosynthetic Processes

Consistent with our previous reports, *Cyld* expression was higher and *Cd34* levels were lower in dHSCs, as confirmed by qPCR (Figures 1E and S1E) (Tesio et al., 2015; Wilson et al., 2008). Other reported HSC markers, such as *Sca-1* and *Epcr/Procr*, or the recently described MolO stem cell signature (Figures 1E and S1F) (Wilson et al., 2015) were also higher expressed in dHSCs compared to aHSCs and MPP1. Moreover, the long non-coding RNA *Meg3* was expressed specifically in dHSCs, while *Pf4* and *Myc* become upregulated in aHSCs and MPP1 (Figures 1E and S1E). Next, we investigated biological pathways differentially represented between dHSCs, aHSCs, and MPP1 using a competitive pathway enrichment analysis (Figures 1F, 1G, and S1G; FDR <0.1). dHSCs were molecularly enriched in immune-related processes such as chemokine signaling pathway, consistent with a likely immune protection of dHSCs against pathogens (Figure 1F). Peptide GPCRs and prostaglandin synthesis and regulation were also enriched in dHSCs (Figure 1F). By contrast, we found a robust downregulation of essential biosynthetic processes such as mRNA processing, eukaryotic transcription initiation, and translation factors in dHSCs compared to aHSCs and MPP1 (Figure 1G). This was associated with the downregulation of *Myc* target genes in dHSCs (FDR <0.1; Figure S1G). These results suggest that reduced biosynthetic activity and a specific immune protection program distinguish dHSCs from the quiescent aHSCs.

Transition from dHSCs to aHSCs Occurs Gradually

Next, we applied single-cell (SiC) RNA-seq to 384 dHSCs and HSCs (HSCs = dHSCs plus aHSCs). We FACS-purified dHSCs or HSCs from SCL mice chased for 150 days with DOX in six independent experiments (Figures 2A and S2A–S2C). Interestingly, when visualizing the set of 319 SiCs that passed quality controls using clustering methods such as a hierarchical clustering heatmap, two-dimensional t-SNE representations, and PCA, we found no evidence for distinct clusters (Figures S2D–S2F; STAR Methods). Thus, we hypothesized that the transition from dormant toward active HSCs follows gradual changes through a series of intermediate cellular states rather than by a binary switch on/off pattern. We then used a computational approach based on pseudo-time analysis (Haghverdi et al., 2016) together with diffusion maps to establish an order of the cells (see the STAR Methods). This revealed dHSCs at the right end of the diffusion map and active HSCs at the left end of the map (Figure S2G) (Haghverdi et al., 2015). We next subdivided cells into four stages (1–4) based on their pseudotime (Figure 2C). dHSCs were most strongly enriched in early stages 1 and 2, while the majority of HSCs occurred in late stages 3 and 4, in line with the notion that these represent predominantly aHSCs. We also observed similar topology and ordering when analyzing the unseparated HSC population only (excluding sorted dHSCs), strongly suggesting that the established organization captures the transition from dHSCs to aHSCs (Figure S2H).

We next quantified the activity of different pathways and assessed variation across the four stages (Figures 2D and S2I–S2M; FDR <0.1). This analysis revealed 19 differentially regulated processes, the majority of which (15/19) exhibited patterns of gradually increased activity from dHSC stage 1 toward aHSC stage 4 cells (Figures 2D and S2I–S2K). These included pathways associated with different cellular biosynthetic activities (such as mRNA processing and translation factors) (Figures 2D and S2I), but also processes such as cell cycle-related pathways (DNA replication, G1 to S cell-cycle control) (Figure S2J) and tumor necrosis factor alpha (TNF-α) nuclear factor κB (NF-kB) signaling (Figure S2K). Confirmatory, the recently described *MolO* stem cell signature (Wilson et al., 2015) showed increased expression from the most dormant toward the most active HSCs (Figures 2E and 2F). Finally, three pathways, such as type II interferon and inflammatory signaling, did not show a continuous increase or decrease suggesting that these processes might act similarly in dormant and aHSCs (Figure S2L). Together, these results indicate that the global transition from inactive dHSCs (stage 1) to aHSCs (stage 4) can be best described by a continuous stream-like progression of steadily increasing metabolic activity and preparation for cell-cycle entry without the apparent presence of accumulating cellular intermediates.

Active HSCs Are Quiescent but Cell-Cycle Primed

To identify individual drivers of variability from dHSCs toward aHSCs, we performed a PCA analysis on all variable genes. We then used different maps to visualize both genes driving differences in PC-1 (e.g., *Ly6a*, *Cdk6*; Figure S2N; for PCA see Figure S2D) and, in addition, canonical marker genes (e.g., *Myc*; Table S2). While *Egr1*, *Ifitm1*, and *Ly6a* expression are steadily decreasing, *Cdk4*, *Cdk6*, and *Myc* expression are steadily increasing at the single-cell level during the transition toward aHSCs (Figures 2G and 2H). Because genes driving differences in PC-1 were mainly cell-cycle activators such as *Cdk6* and *Nap1l1* (Figure S2N), we bioinformatically assessed the cell-cycle signature and cell-cycle stage of each individual cell (Figures 2I–2K, S2O, and S2P) (Scialdone et al., 2015). Consistent with the notion that both dormant and active HSCs are quiescent, all cells were classified as G_0/G_1. Similarly, the distribution of the probability for being in the G_0/G_1 phase was comparable across stages of pseudo-time (Figure S2O). Next, to investigate evidence for subtle variations in cell-cycle stages between dHSCs and aHSCs, we applied PCA to a set of genes that are annotated to cell cycle finding higher expression of cell-cycle

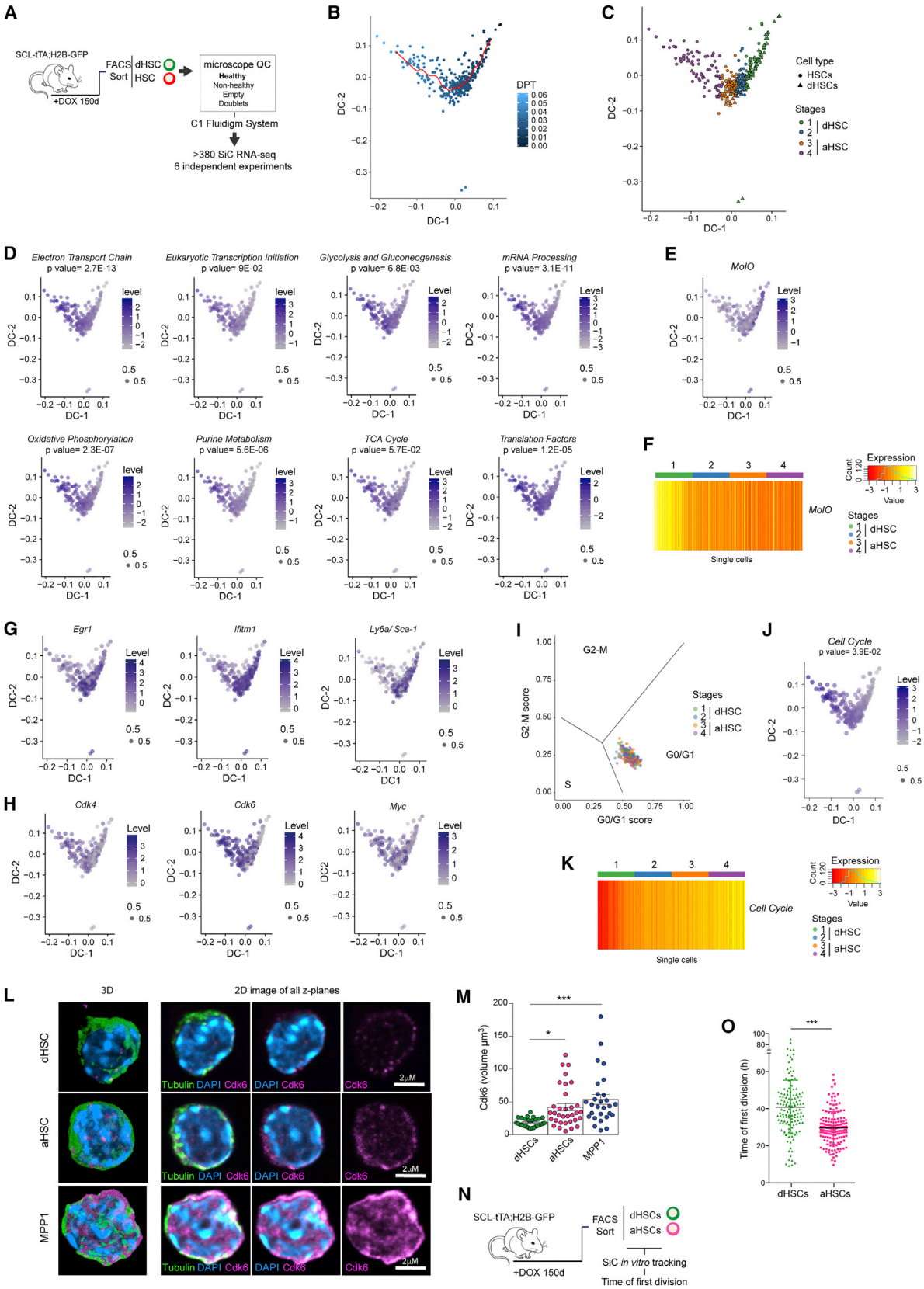

(legend on next page)

genes in stage 4 aHSCs (Figures 2J, 2K, and S2P). We investigated individual members of the cell-cycle pathway in greater detail using population RNA-seq data of dHSC, aHSC, and MPP1 (Figure S2Q; Table S1). In line with the global Cyclone approach (Figure 2I), most genes related to DNA replication (*Cdc45*, *Mcm4*) were similarly low in dHSCs and aHSCs. In contrast, *p57* was higher in dHSCs compared to aHSCs and MPP1, while *Cdk4* increased its expression in aHSC and MPP1. These observations show that while dHSCs and aHSCs are both quiescent (both G_0/G_1), aHSCs are cell-cycle primed and major regulators that are differentially expressed in dormant and active HSCs may be involved in retaining HSCs dormancy.

As Cdk6 protein expression has recently been linked to a quiescent state primed to cell-cycle entry (Laurenti et al., 2015), we investigated its expression in dHSCs, aHSCs, and MPP1 by immunofluorescence (Figures 2L and 2M). Briefly, we scanned Cdk6 expression in 89 FACS-sorted single cells by confocal microscopy, generated 3D images, and quantified the volume of protein signal. Cdk6 expression was homogeneously very low in dHSCs, while individual cells within the aHSC and MPP1 population expressed higher Cdk6 levels. In addition, overall levels of Cdk6 steadily increase from dHSCs to aHSCs and MPP1 (Figures 2L and 2M) in line with studies in human long-term and short-term HSCs (Laurenti et al., 2015).

To functionally explore the differences in the cell-cycle entry kinetics between the dormant and the active/quiescent state, we performed SiC in vitro tracking analysis (Figures 2N and 2O) (Haetscher et al., 2015; Rieger et al., 2009). We FACS-sorted dHSCs and aHSCs and calculated the time to first division of 285 SiCs by live cell imaging. Interestingly, aHSCs showed an average of 29.5 ± 0.7 hr to generate the first progeny, while dHSCs needed 40.8 ± 1.3 hr. This pronounced difference (11.3 hr) between two initially non-cycling populations suggests that dHSCs reside in a deeper level of quiescence.

Altogether, these results show that protein synthesis and cell-cycle-related components increase in HSCs exiting dormancy and moving toward the active state. Although aHSCs have not yet entered the cell cycle and thus are still considered quiescent, they are already primed toward more active metabolic and cell-cycle-related pathways.

Isolation of Viable dHSCs Using the Gprc5c-EGFP Reporter Mouse

So far, reliable identification and ex vivo isolation of dHSCs has been only possible using time-consuming LRC assays performed in inducible H2B-GFP expressing mouse lines by labeling cells with bromodeoxyuridine (BrdU) or Carboxyfluorescein succinimidyl ester (CFSE) (Bernitz et al., 2016; Foudi et al., 2009; Qiu et al., 2014; Takizawa et al., 2011; Wilson et al., 2008). Because several mouse models enabling HSC identification have recently been generated (Acar et al., 2015; Chen et al., 2016; Gazit et al., 2014a), we first investigated whether their expression is also specific for dHSCs (Figure S3A). Although the expression of all the reported HSC markers is higher in HSC and HSC-MPP1 compared to late MPPs, none of them has a robust differential expression in dHSCs. Thus, to identify dHSC-specific cell surface markers, we searched our RNA-seq expression data (dHSC versus aHSCs) and classified all expressed genes enriched in dHSCs according to their protein class (FDR <0.1; Figure S3B). Among other receptors and cell adhesion molecules, the surface receptor, *Gprc5c* (G protein-coupled receptor, class C, group 5; retinoic acid-induced gene 3 [*Raig3*]) was higher expressed in dHSCs compared to aHSCs and MPP1 (Figure 3A). *Gprc5c* encodes an orphan G protein-coupled receptor (Robbins et al., 2000) that activates intracellular heterotrimeric G proteins (Pierce et al., 2002). Expression analysis including the MPP1–MPP4 subsets confirmed its low expression in early progenitors as shown by RNA-seq (Figure 3B) (Cabezas-Wallscheid et al., 2014) and qPCR (Figure S3C). To corroborate and extend these findings, we employed a bacterial artificial chromosome (BAC) transgenic reporter mouse line expressing EGFP under the control of the *Gprc5c* promoter (Gprc5c-EGFP) (Figure 3C; STAR Methods). We characterized the activity of the *Gprc5c* promoter in the HSC-MPP compartment by measuring EGFP expression (Figures 3D, S3D, and S3E). In line with the presence of 20%–30% of dHSCs within the adult HSC compartment and our RNA expression profiles (Figure 1A) (van der Wath et al., 2009; Wilson et al., 2008), we observed that 27.9% ± 8.1% of all HSCs expressed EGFP under the control of the Gprc5c promoter (hereafter named Gpr^{pos}). In contrast, only 3.0% ± 1.8% of MPP1 and 1.6% ± 0.3% of other MPPs were Gpr^{pos}. In agreement with data linking higher CD150 expression to increased HSC

Figure 2. Single-Cell RNA-Seq of dHSCs and HSCs

(A) Simplified SiC RNA-seq workflow. For full details, see Figure S2A and the STAR Methods.

(B) Pseudo-time plot showing pseudotemporal ordering of cells and their location in the diffusion map. DPT, diffusion pseudo time. DC-1, 2, diffusion component 1, 2.

(C) Diffusion map representation. Coloring is derived from partitioning DPT into four stages: most dormant (stage 1) toward most active HSCs (stage 4).

(D and E) Diffusion map representation of biosynthesis signaling pathways (D) and *MolO* signature (E). Colors encode standardized pathway activity. FDR <0.1.

(F) Heatmap based on the expression of *MolO*-related genes. Each line represents one cell.

(G and H) Diffusion map representation of single genes. Genes that change expression from most dHSCs (stage 1) towards aHSCs (stage 4). (G) Genes highly expressed in dHSCs decrease their expression towards aHSCs. (H) Genes lowly expressed in dHSCs increase their expression towards aHSCs. Colors encode standardized gene expression.

(I) Cell-cycle status distribution. Each individual cell is positioned according to their G_0/G_1 and G_2/M score.

(J) Diffusion map representation of the expression of cell-cycle-related genes. Colors encode normalized pathway activity.

(K) Heatmap based on the expression of cell-cycle-related genes. Each line is one cell.

(L and M) Cdk6 expression. (L) Immunofluorescence images. Tub, Tubulin. (M) Quantification of Cdk6 expression. N = 3.

(N and O) Single-cell (SiC) in vitro tracking. (N) Workflow. (O) Quantification. N = 3.

For (J) and (K), ± SEM is shown. *p <0.05; ***p <0.001. N indicates biological replicates. For further details, see the STAR Methods. Each dot represents one cell for (B–E), (G–I), (K), (M), and (O). Of note, HSCs include dHSCs and aHSCs. SiC, single-cell. See also Table S2.

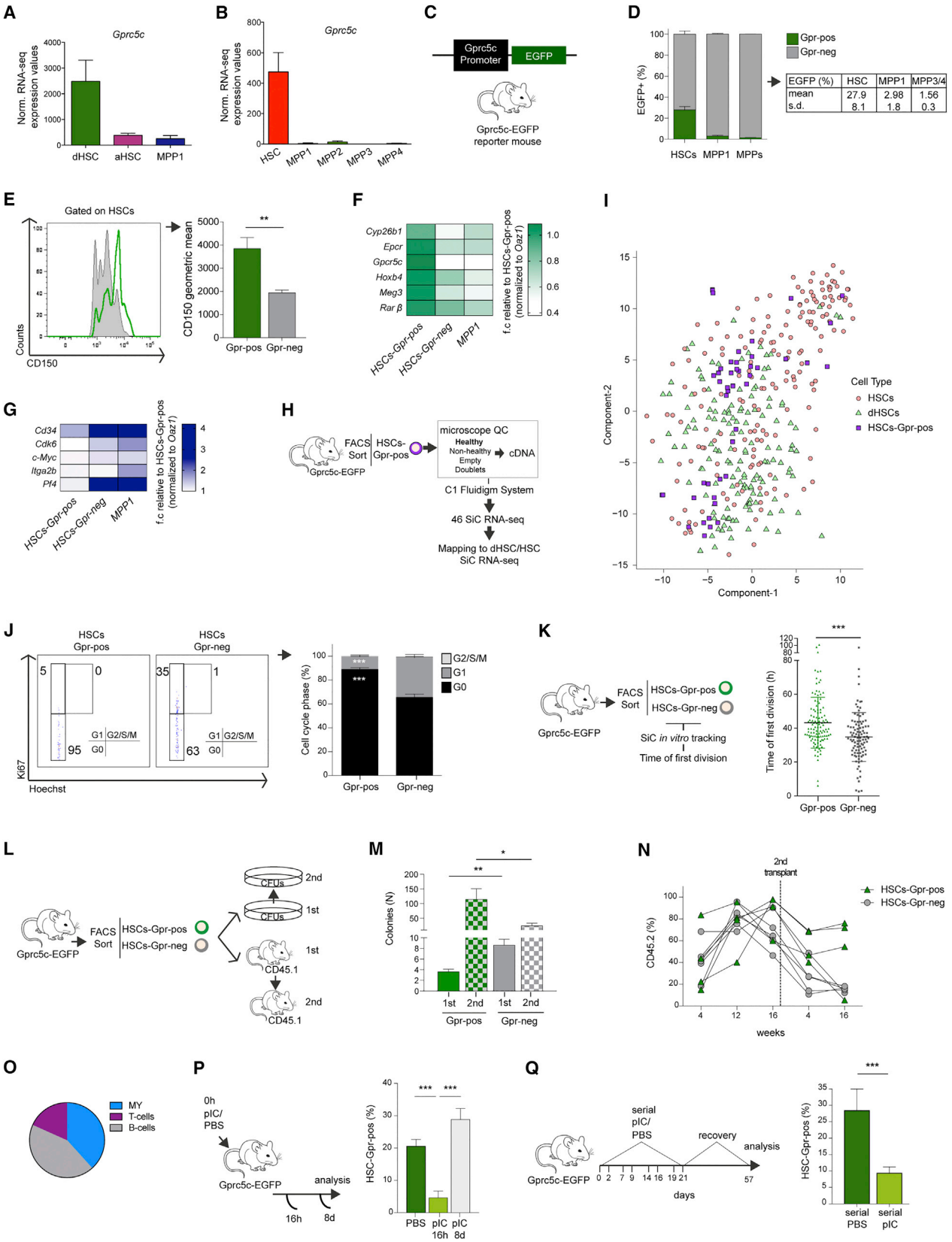

(legend on next page)

potency, HSC-Gpr^{pos} cells expressed 2-fold higher levels of cell surface CD150 compared to HSC-Gpr^{neg} (Figure 3E) (Beerman et al., 2010; Morita et al., 2010). To associate Gpr expression to other stem cell markers, we pre-gated on LSKCD34$^-$ Gpr^{pos} or Gpr^{neg} cells and then investigated the enrichment on CD150$^+$CD48$^-$ stem cells (Figures S3F and S3G). Strikingly, we found that Gpr^{pos} pre-gated cells were four times enriched for CD150$^+$CD48$^-$. To address molecular similarities between HSCs-Gpr^{pos} and dHSCs, we compared expression of dHSC-specific markers and other genes in HSCs-Gpr^{pos}, HSCs-Gpr^{neg}, and MPP1 by qPCR analysis (Figures 3F, 3G, and S3H). Consistently, we found *Meg3*, *Cyp26b1*, *Gprc5c*, *Procr/Epcr*, *Cyp26b1*, and *Rar*β higher and *CD34*, *Itga2b*, and *Pf4* lower expressed in HSCs-Gpr^{pos}. Thus, HSC-Gpr^{pos} cells and dHSCs isolated by LRC assays show a highly overlapping molecular signature.

Next, we generated single-cell RNA-seq of 52 HSC-Gpr^{pos} cells and mapped these to the SiC RNA-seq data of dHSCs/HSCs (Figures 3H, 3I, S3I, and S3J). We found an enrichment of HSCs-Gpr^{pos} clustering within dHSCs, indicating that the global molecular fingerprints of HSCs-Gpr^{pos} resemble those of dHSCs. Cell-cycle analysis (Figure 3J) and SiC in vitro tracking assays (Figure 3K) showed that HSC-Gpr^{pos} are more quiescent and require more time for their first division compared to HSCs-Gpr^{neg} cells. Serial colony-forming unit (CFU) assays and transplant experiments (Figures 3L–3O) showed that HSCs-Gpr^{pos} formed significantly more colonies than HSCs-Gpr^{neg} cells in secondary platings (Figure 3M) and an improved outcome in secondary transplantations compared to HSCs-Gpr^{neg} transplanted animals indicating higher self-renewal capacities (Figure 3N). HSCs-Gpr^{pos} were multipotent giving rise to myeloid and lymphoid lineages (Figures 3O and S3K). To functionally validate HSC-Gpr^{pos} cells as a reversible dHSC population in vivo, we stimulated Gprc5c-EGFP mice with the double-stranded RNA analog polyI:polyC (pIC) mimicking viral infection and measured EGFP expression 16 hr and 8 days after stimulation (Figure 3P) (Essers et al., 2009). The proportion of HSC-Gpr^{pos} cells decreased from 20.5% ± 2.2% during homeostatic conditions to 6.2% ± 1.4% 16 hr after pIC treatment (see also Figure S3L), but returned to initial levels (28.8% ± 3.5%) after a recovery period of 8 days. To address the behavior of dHSCs upon serial stress stimulation, we serially treated Gpr-EGFP mice with pIC and measured the HSC-Gpr^{pos} levels 4 weeks after stimulation (Figures 3Q, S3M, and S3N). We found that the HSC-Gpr^{pos} compartment was reduced compared to the PBS-treated group suggesting incomplete recovery of dHSCs after long-term stress stimulation. Taken together, these results show that HSC-Gpr^{pos} cells display similar molecular and functional properties as dHSCs, demonstrating that the Gprc5c-EGFP reporter mouse line is a valid alternative tool to track dHSCs and thus circumvent LRC assays. In addition, the reversibility of the Gprc5c-EGFP system allows a flexible analysis of the dHSC compartment in homeostatic and stress-induced settings.

All-*trans* Retinoic Acid Treatment Maintains dHSCs In Vitro

By examining our RNA-seq dataset, we found that retinoic acid (RA)-induced signaling was highly enriched in dHSCs compared to aHSCs and MPP1 (Figures 4A and 4B), confirming and extending our recent findings on HSC-MPPs (Cabezas-Wallscheid et al., 2014) (Figure S4A).

To functionally address the role of RA signaling in dHSCs, we cultured hematopoietic stem/progenitor cells (HSPCs) isolated from Gpr-EGFP mice with activating conditions in the presence or absence of the RA signaling agonist all-*trans* retinoic acid (ATRA). ATRA-treated HSCs showed significantly higher retention of EGFP levels (measure of dormancy) compared to untreated conditions (Figures 4C, 4D, S4B, and S4C). Cell viability upon ATRA treatment was unaffected in HSCs as shown by measurement of active caspase-3 (Figure S4D). In agreement, maintenance of dHSC/LRCs (GFP$^+$ cells) isolated from SCL-tTA;H2B-GFP mice DOX-chased for 150 days was enhanced, and cells remained in a GFP$^+$ state in the presence of ATRA

Figure 3. Gprc5c-EGFP Reporter Mouse Model

(A) RNA-seq expression of Gprc5c from dHSCs to MPP1. Population normalized RNA expression values (arbitrary units). N = 3.

(B) RNA-seq expression of Gprc5c from HSCs to MPP4. Normalized RNA expression values (arbitrary units), data based on Cabezas-Wallscheid et al. (2014). N > 3.

(C) Gprc5c-EGFP reporter mouse model. Expression of EGFP under the activity of the Gprc5c promoter.

(D) Activity of the Gprc5c promoter in the early adult hematopoietic compartment. Percentage of EGFP within each population is represented. Gated on HSCs (LSK CD150$^+$CD48$^-$CD34$^-$), MPP1 (LSK CD150$^+$CD48$^-$CD34$^+$), and MPP3/4 (LSK CD150$^+$CD48$^+$). N = 7. More than three independent experiments.

(E) Expression of CD150 within Gpr^{pos} or Gpr^{neg} HSCs. Geometric mean of CD150 fluorescence is represented. Gated on HSCs (LSK CD150$^+$CD48$^-$CD34$^-$). N = 3. Two independent experiments.

(F and G) Differential gene expression. Heatmap representing RNA expression based on qPCR data (normalized to housekeeping genes). (F) Higher expressed in HSCs-Gpr^{pos}. (G) Higher expressed in HSCs-Gpr^{neg}. N = 5–6. Greater than or equal to two independent experiments.

(H) Single-cell RNA-seq workflow.

(I) TSNE-based visualization and clustering of HSC-Gpr^{pos} single-cell RNA-seq data. Sorted HSCs-Gpr^{pos} (quadrants), HSCs (circles), and dHSCs (triangles). Two independent experiments.

(J) Cell-cycle analysis. Left: representative FACS plots. Right: percentage within each cell-cycle phase. N = 6. Greater than two independent experiments.

(K) Single-cell (SiC) in vitro tracking. Left: workflow. Right: SiC tracking results. Each dot represents one cell. N = 3.

(L–O) Functional experiments. (L) Workflow. (M) Colony-forming unit assay (CFU). Total colonies are represented for the first and second plating. N = 5. Two independent experiments. (N) Transplantation experiments. CD45.2% outcome is represented. N = 4–5. Each dot represents one mouse. (O) Multipotency. Relative outcome of myeloid and lymphoid (B and T cells) in peripheral blood of HSC-Gpr^{pos} 16 weeks after first transplant. N = 4.

(P) HSC activation and reversibility. Left: workflow. Right: percentage of EGFP within HSCs is represented. N = 3–5. Two independent experiments.

(Q) Serial HSC activation and reversibility. Left: workflow. Right: percentage of EGFP within HSCs is represented. N = 4. For all panels, ±SEM is shown. *p <0.05; **p < 0.01; ***p <0.001. N indicates biological replicates.

See also Figure S3.

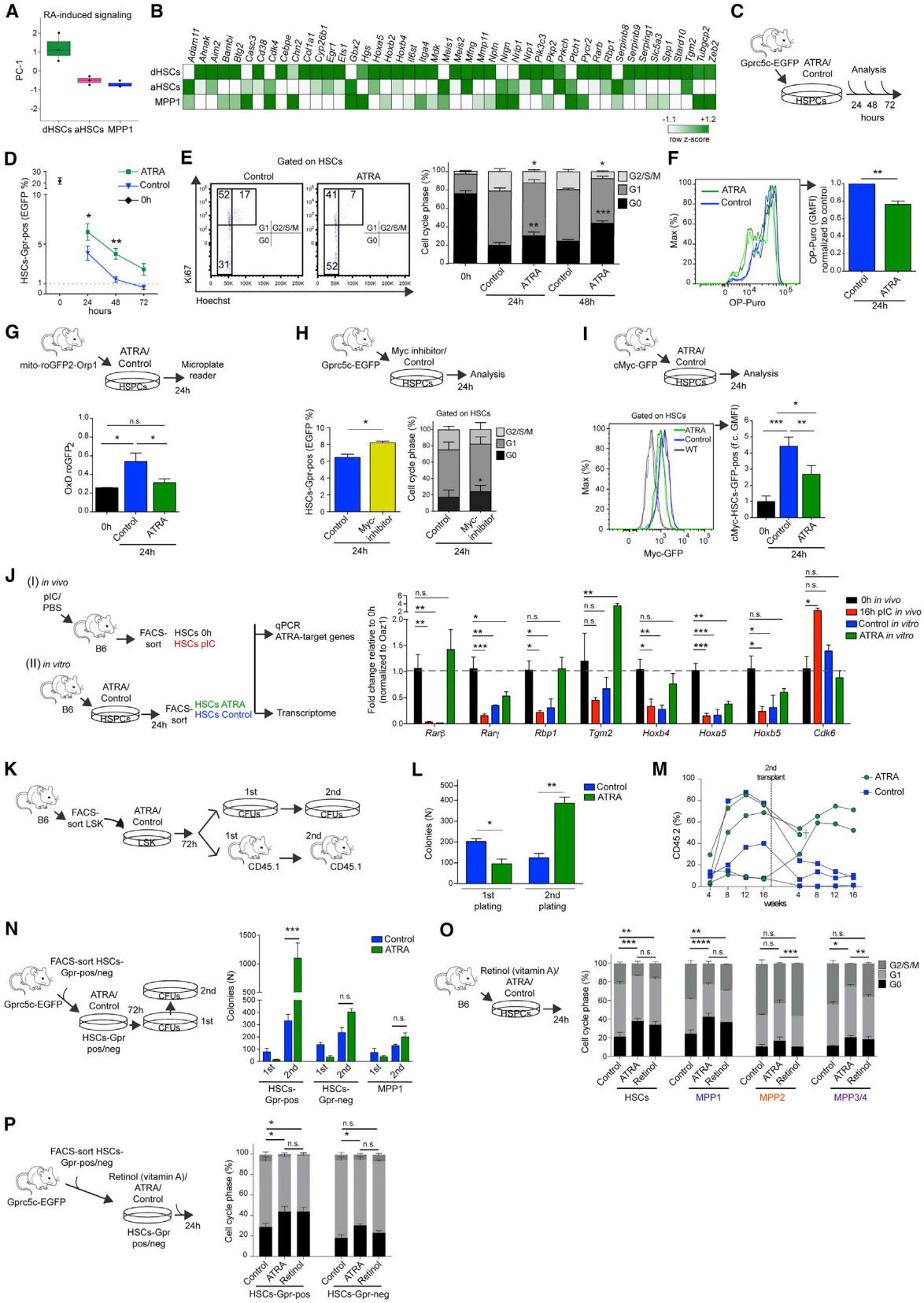

(legend on next page)

in vitro (Figure S4E). Cell-cycle profiles measured by Hoechst/Ki67 staining revealed that HSCs cultured with ATRA were significantly more quiescent (Figures 4E and S4F). To assess whether the observed cell-cycle phenotype is dependent on other progenitor cells, we FACS-sorted phenotypic HSCs and cultured them with ATRA (Figure S4G). Purified ATRA-treated HSCs exhibited a cell-cycle arrest, indicating a cell-autonomous effect.

An overall low biosynthetic activity was a major difference between the transcriptional profile of dHSCs and their progeny (Figure 1G). To evaluate whether RA signaling has an effect on translation, we used a membrane-diffusible alkaline analog of puromycin, O-propargyl-puromycin (OP-Puro) to explore de novo protein synthesis (Liu et al., 2012; Signer et al., 2014). We observed a 24% decrease in OP-Puro incorporation in ATRA-treated HSCs, suggesting lower nascent protein translation rates upon active RA signaling (Figure 4F). Low levels of reactive oxygen species (ROS) linked to low use of oxidative phosphorylation as an energy source have also been associated with homeostatic HSC quiescence (Ludin et al., 2014; Suda et al., 2011). To quantify relative differences in ROS levels in intact living cells, we employed transgenic mice globally expressing mito-roGFP2-Orp1 (Fujikawa et al., 2016), a genetically encoded H_2O_2-sensitive probe targeted to the mitochondrial matrix (Figures 4G and S4H). Strikingly, we observed a strong reduction of the mitochondrial sensor upon ATRA treatment, back to a level similar to the ex vivo uncultured samples (Figures 4G and S4H). Taken together, these results show that RA signaling retains HSC quiescence in activating cell culture conditions by maintaining low translation rates and preventing increase of ROS.

ATRA-treated HSCs mimicked a dormant state recently described in Myc-depleted embryonic stem cells, characterized by low proliferation and biosynthesis (Scognamiglio et al., 2016). In line, c-Myc levels were low in dHSCs but increased in aHSCs (Figure 2H). Thus, we cultured HSPCs from Gpr-EGFP mice with the Myc/Max inhibitor 10058-F4 (Zirath et al., 2013). We found slightly higher numbers of HSC-Gpr^{pos} retained in a more quiescent state, partially mimicking the effects of ATRA (Figure 4H). To address whether c-Myc protein is regulated by RA signaling, we used the c-Myc-GFP reporter mouse model (Figure 4I) (Huang et al., 2008). ATRA treatment significantly attenuated the c-Myc-GFP upregulation upon culture, and this effect was not synergistic as shown by combining ATRA and MYCi treatments (Figure S4I). In summary, our results show that ATRA treatment retains low levels of c-Myc, and inhibition of Myc activity partially mimics the preservation of dormancy by ATRA, indicating that ATRA may preserve dormancy by restricting Myc.

To assess the preservation of molecular fingerprints of HSCs, we addressed differential expression signatures upon in vitro ATRA treatment and compared these to non-cultured HSCs (0 hr) as well as in vivo stressed-HSCs (16 hr after a single pIC injection) (Figures 4J, S4K, and S4L; Table S3). As expected, target genes of the RA pathway such as *Tgm2*, *Rbp1*, and *Gprc5c* were upregulated or maintained upon ATRA treatment compared to the in vitro control and the stressed in vivo group (Figure 4J). In accordance with the observed cell-cycle arrest (Figure 4E), *Cdk6* expression was reduced in ATRA-treated cells, while the self-renewal-associated *Hoxb4* gene (Antonchuk et al., 2001) was maintained in response to ATRA. Rarγ was downregulated in ATRA- and non-ATRA-treated HSCs while Rarα was not detected (data not shown). In contrast, Rarβ expression was entirely depleted in control samples but maintained at physiological levels upon ATRA treatment. These data were supported by our RNA-seq expression analysis, showing that the Rarβ receptor (in contrast to Rarγ and Rarα) is specifically expressed in dHSCs compared to aHSCs and MPP1 (Figure S4J). Further, microarray-based global transcriptome analysis showed that ATRA-treated cells presented a robust downregulation of G2M checkpoints, E2F targets, ROS species, and Myc targets compared to untreated cells (Figure S4L), supporting our previous findings (Figures 4C–4I). Because Gprc5c-KO HSPCs do

Figure 4. Role of Retinoic Acid in dHSCs In Vitro

(A) PCA. Expression pattern of a retinoic acid (RA)-induced signaling signature at the population level (Balmer and Blomhoff, 2002). First principal component on RA-induced genes is represented.

(B) Heatmap of RA-induced signaling. RNA-seq data were mapped to a RA-induced signaling signature (Balmer and Blomhoff, 2002). Heatmap representing *Z* scores of RNA-seq normalized expression values. Only genes with >500 counts are depicted. N = 3.

(C and D) *Gprc5c* expression upon in vitro ATRA treatment. (C) Workflow. (D) Percentage of EGFP within HSCs is represented. N = 4–5.

(E) Cell-cycle analysis upon in vitro ATRA treatment. Left: representative FACS dot plot. Gated on LSK CD150$^+$CD48$^-$CD34$^-$. Right: relative percentage within each cell-cycle phase. N = 3–6.

(F) Translation rate analysis by OP-Puro uptake. Left: representative FACS histogram plot. Gated on LSK CD48$^-$CD34$^-$. Right: geometric mean fluorescence intensity (GMFI) is represented. N = 3.

(G) Mitochondrial H_2O_2. Top: workflow. Bottom: degree of oxidation of mito-roGFP2-Orp1 (OxD) is represented. N = 3.

(H) Gprc5c activity upon in vitro Myc-inhibitor treatment. Top: workflow. Bottom: fold change of EGFP and relative percentage within each cell-cycle phase within HSCs is represented. N = 3.

(I) Myc activity upon in vitro ATRA treatment. Top: workflow. Bottom: percentage of Myc-GFP within HSCs is represented. Gated on LSK CD150$^+$CD48$^-$CD34$^-$. N = 3.

(J) Molecular targets of in vitro ATRA treatment. Left: Workflow. Right: qPCR of RA targets genes and cell-cycle regulators upon culture relative to 0 hr untreated HSCs. N = 3. Of note, microarray transcriptome data in Figures S3K and S3L.

(K–M) Functional experiments. (K) Workflow. (L) Colony-forming unit assay (CFU). Total colonies are represented for the first and second plating. N = 3. (M) Transplantation experiments. CD45.2% outcome is represented. N = 3–4. One independent experiment.

(N) HSC-Gpr$^{pos/neg}$ colony-forming unit assay (CFU). Left: Workflow. Right: total colonies are represented for the first and second plating. N = 5–6.

(O) Cell-cycle analysis upon in vitro retinol treatment. Left: workflow. Right: relative percentage within each cell-cycle phase. N = 2.

(P) Cell-cycle analysis of HSC-Gpr$^{pos/neg}$ upon in vitro retinol treatment. Relative percentage within each cell-cycle phase. N = 4–6. For all panels, ±SEM is shown. *p <0.05; **p <0.01; ***p <0.001. n.s., not significant. N indicates biological replicates. For all experiments greater than or equal to two independent experiments were performed unless otherwise indicated.

See also Figure S4 and Table S3.

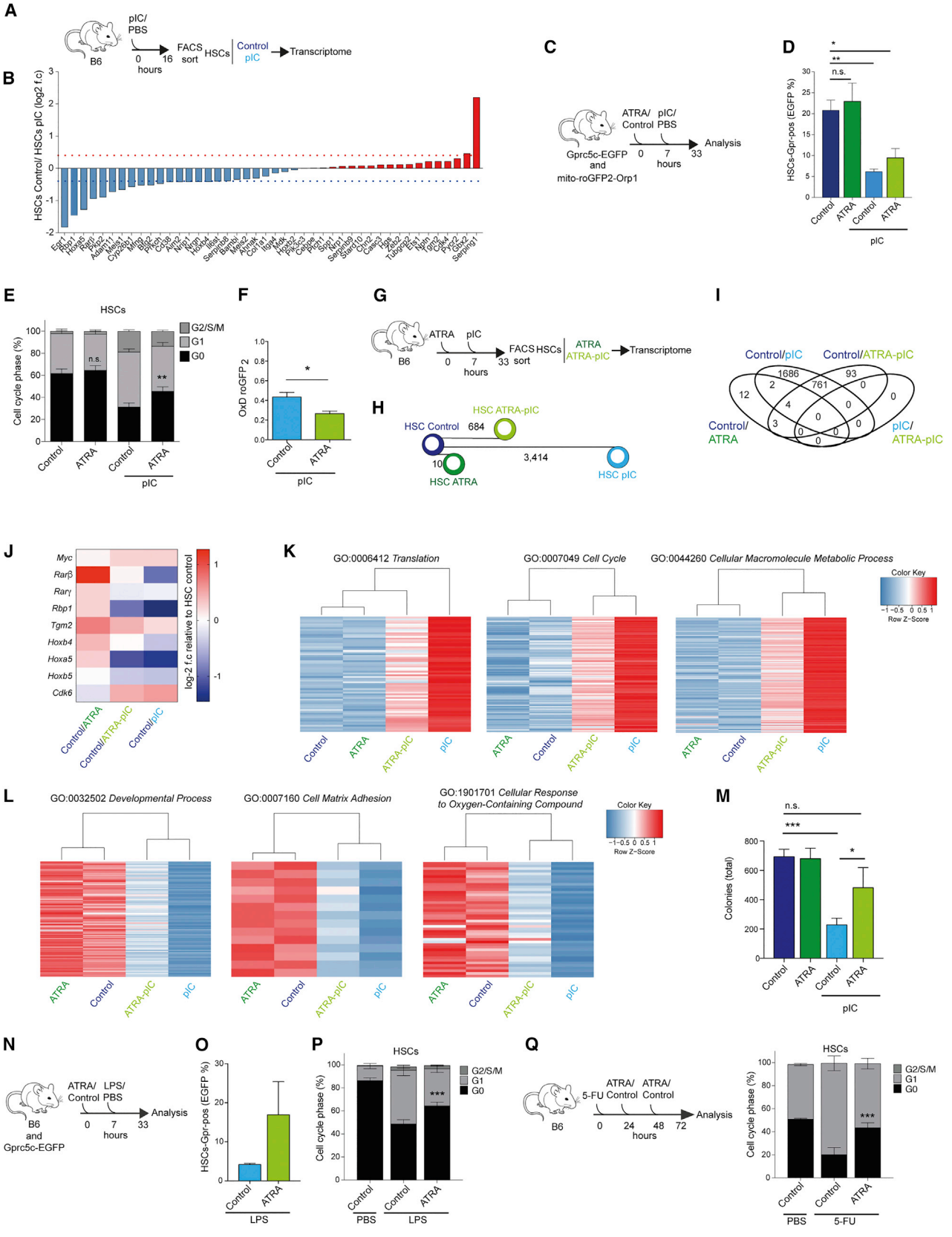

(legend on next page)

respond to ATRA treatment, Gprc5c itself is not mediating the observed cell-cycle effects (Figure S4M).

We next performed serial plating CFU assays and transplantation experiments (Figures 4K–4M). ATRA-treated cells formed significantly more colonies in the second plating and also performed better in subsequent serial reconstitution experiments compared to control cells (Figures 4L and 4M). To address whether the observed effect is dHSC-specific, we cultured FACS-sorted HSCs-Gpr^{pos} and HSCs-Gpr^{neg} in the presence or absence of ATRA and performed CFU re-plating assays (Figure 4N). ATRA treatment considerably increased the HSC-Gpr^{pos} number of colonies in the secondary plating compared to both untreated and ATRA-treated HSCs-Gpr^{neg}. These results argue for a distinct role of RA signaling in HSCs-Gpr^{pos} cells and are in line with the molecular signatures, in vivo transplants, and in vitro CFU assays (Figures 4K–4N). Together, ATRA treatment retains the long-term self-renewal capabilities of dHSCs in vitro.

Because ATRA is the biologically active metabolite of vitamin A (retinol) (Collins, 2008), we next addressed whether HSCs are able to metabolize vitamin A-retinol. First, HSPCs were cultured with retinol and cell-cycle profiles were assessed (Figures 4O and S3N). MPP2 and MPP3/4 did not display the expected cell-cycle arrest observed upon in vitro ATRA treatment suggesting that these populations are not able to metabolize retinol. By contrast, HSCs and MPP1 showed similar cell-cycle arrest as observed upon ATRA treatment. Next, we addressed whether the observed effect is dHSC-specific and cell-autonomous by culturing FACS-sorted HSCs-Gpr^{pos} and HSCs-Gpr^{neg} (Figure 4P). HSCs-Gpr^{pos} showed higher cell-cycle arrest compared to HSCs-Gpr^{neg} in all conditions.

Collectively, these data show that ectopic RA signaling can maintain HSC quiescence even in activating culture conditions by retaining low translation, proliferation, ROS levels and c-Myc protein levels. Moreover, external vitamin A-retinol can be metabolized by dHSCs in a cell-autonomous manner.

ATRA Treatment Retains Dormancy and Reduced Levels of ROS in Response to Stress-Mediated Activation Signals In Vivo

Based on the results above, we hypothesized that activation of HSCs in vivo with treatments such as pIC should lead to downregulation of RA signaling. We treated mice with PBS or pIC and 16 hr later FACS-sorted HSCs and performed transcriptome analysis (hereafter termed HSCs-Control and HSCs-pIC, respectively) (Figures 5A and 5B; Table S4). Most of the RA-induced genes were downregulated upon pIC treatment. Next, we pre-treated either Gpr-EGFP or mito-roGFP2-Orp1 mice with ATRA followed by a single pIC injection to investigate whether ATRA pre-treatment would prevent dHSCs from cell-cycle entry (Figure 5C). Neither the percentage of HSC-Gpr^{pos} cells nor cell-cycle profiles were changed by short-term ATRA treatment during homeostasis (Figures 5D and 5E). As expected, we observed an induction of Sca-1 expression within the LSK population after pIC injections in control and ATRA-treated groups (Figures S5A and S5B) (Essers et al., 2009). In contrast, ATRA pre-treatment caused a preservation of HSC-Gpr^{pos} cells in response to pIC treatment (Figure 5D). In agreement, ATRA-treated HSCs were kept in a more quiescent G_0 state as determined by cell-cycle analysis (Figures 5E and S5A). Of note, this was not observed in MPPs indicating that ATRA-mediated effects are HSC-specific and no changes in HSC-MPP frequencies were observed (Figures S5C and S5D). Furthermore, HSCs from ATRA-treated mice showed a lower degree of oxidation upon exposure to stress stimuli (Figure 5F). Next, we performed microarray-based transcriptome analysis on HSCs isolated from pre-treated ATRA mice followed by pIC injection (hereafter termed HSCs-ATRA and HSCs-ATRA-pIC, respectively) (Figure 5G; Table S4) and compared their transcriptome to HSCs-Control and HSCs-pIC (Figures 5A, 5H, and S5E). HSCs-Control and HSCs-ATRA were transcriptionally similar (10 differentially expressed genes [DEG]; Figures 5H and 5I) in line with our previous observation on unchanged HSC-Gpr^{pos} numbers and cell-cycle profiles (Figures 5D and 5E). As expected, HSCs-Control and HSCs-pIC showed robust transcriptional differences (3,414 DEG). Strikingly, these differences were strongly reduced when comparing HSCs-Control to HSCs-ATRA-pIC (684 DEG). RA target genes (Figure 5J) and global processes (cell cycle, developmental processes; FDR <0.1; Figures 5K and 5L) were partially rescued by ATRA pre-treatment. GSEA analysis revealed a significant downregulation of Myc targets, G2M checkpoint, and an upregulation of RA-induced signaling in HSCs-ATRA-pIC compared to HSCs-pIC (Figure S5F). Next, we performed CFU

Figure 5. In Vivo Role of Retinoic Acid in dHSCs

(A and B) Retinoic acid (RA) signaling upon stress response. (A) Workflow. Generation of transcriptome data from pIC-treated HSCs. (B) Transcriptome changes of RA-induced signaling upon pIC-induced stress. RA signature based on Balmer and Blomhoff (2002). Arbitrary cutoff in ± 0.3 log2 fold-change (f.c).

(C–F) In vivo ATRA and pIC treatment. (C) Workflow. (D) HSC-Gpr^{pos} analysis. Percentage of EGFP within HSCs is represented. N = 5. (E) Cell-cycle analysis. Relative percentage within each cell-cycle phase. N = 5. (F) Mitochondrial H_2O_2. Degree of mito-roGFP2-Orp1 oxidation (OxD) is represented. N = 4.

(G–L) Transcriptome analysis of ATRA-treated HSCs in homeostasis and stress. N = 2–3. (G) Workflow. (H) Closest neighbor analysis. Relative distances are shown based on numbers of differentially expressed genes in pairwise comparisons. (I) Overlapping gene expression. Numbers indicate DE genes in pairwise comparisons. FDR <0.1. (J) Relative expression from Control versus ATRA, ATRA-pIC, and pIC. Heatmap representing log2 fold changes based on microarray data in the indicated pairwise comparisons. (K and L) Differential pathways. Heatmaps representing *Z* scores of microarray normalized expression values. FDR <0.1. N = 2–3. (K) Upregulated in pIC. (L) Downregulated in pIC.

(M) Colony-forming unit assay (CFU). Total colonies are represented. N = 3.

(N–P) in vivo ATRA and LPS treatment. (N) Workflow. (O) Cell-cycle analysis. Relative percentage within each cell-cycle phase. N = 5. (P) HSC-Gpr^{pos} analysis. Percentage of EGFP within HSCs is represented. N = 3. One independent experiment.

(Q) In vivo 5-FU and ATRA treatment. Right: workflow. Left: cell-cycle analysis. Relative percentage within each cell-cycle phase. N = 5. For all panels, HSCs gated on LSK CD150^{+}CD48^{-}CD34^{-}, ±SEM is shown. *p <0.05; **p <0.01; ***p <0.001. n.s., not significant. N indicates biological replicates. For all experiments, greater than or equal to two independent experiments were performed unless otherwise indicated.

See also Figure S5 and Table S4.

assays and found that ATRA treatment did not alter the number of colonies in pIC-untreated cells but it partially rescued the decreased CFU activity of pIC-treated mice (Figure 5M). In summary, the presence of ATRA attenuates pIC-induced HSC activation in vivo.

To investigate whether the retention of ATRA-treated HSCs in dormancy is expandable to other HSC-activation regimen, we treated mice with bacterial liposaccharide (LPS) (Takizawa et al., 2011) (Figures 5N–5P and S5G). Also upon LPS stimulation, ATRA pre-treatment maintained HSC-Gpr^{pos} cells (Figure 5O). In line, HSCs pre-treated with ATRA were maintained in a more quiescent state, and this difference was not observed in MPPs (Figures 5P and S5G). Further, we employed the chemotherapeutic agent 5-fluorouracil (5-FU) to activate HSCs (Figures 5Q, S5H, and S5I) (Venezia et al., 2004). Strikingly, upon 5-FU treatment and in the presence of ATRA, HSCs were retained in a more quiescent state compared to the control group, and this effect was not observed in MPPs. These results demonstrate that RA signaling specifically retains HSC quiescence in mice exposed to diverse HSC activation conditions, including pIC, LPS, and the chemotherapeutic agent 5-FU, and illustrates the potency of RA/vitamin A to prevent cycling and thus maintenance of functional quiescent HSCs not only in culture but also in vivo.

Vitamin A-free Diet Leads to Impaired dHSC Reversibility

To address whether vitamin A-mediated RA signaling is required for HSCs, we fed adult mice with a vitamin A-free diet for 14–17 weeks (hereafter termed vit.A-free; Figure 6A) to deplete the RA reservoir in vivo. White blood cell and lymphocyte counts progressively decreased in vit.A-free mice (Figures 6B and S6A). Body weight and spleen/body ratios were unchanged (Figures S6B and S6C), while bone marrow (BM) cellularity was reduced (Figure S6D). In addition, BM granulocytes were slightly increased, mature B cells were significantly reduced, and splenic LSK frequencies remained unchanged (Figures S6E and S6F). HSC frequency in the bone marrow was significantly decreased (Figure 6C). Similarly, the number of dormant HSC-Gpr^{pos} cells were significantly reduced in a homeostatic vit.A-free environment (Figure 6D). Cell-cycle analysis showed no significant difference between the groups (Figure 6E). However, qPCR analysis of HSCs from vitamin A-starved mice showed downregulation of *Rar*β and *Cyp26b1* expression while other RA target genes (e.g., *Rbp1*, *Cdk6*, and *Hoxb4*) did not change in HSCs nor in MPPs (Figure 6F). Serial CFU assays of vit.A-free BM cells showed decreased number of colonies in serial platings indicating defective long-term self-renewal (third, fourth plating; Figure 6G). In addition, upon transplantation of vit.A-starved bone marrow, the reconstitution potential was decreased suggesting functional impairment of HSCs present in the bone marrow of mice suffering from vit.A-starvation (Figure 6H). Next, we assessed reversibility of dHSCs in a normal and a vit.A-free environment by applying a single pIC injection 8–11 days before analysis (Figures 6I–6L and S6H–S6L). As expected, HSCs in a control environment returned to similar HSC numbers and to a quiescent state 8–11 days after pIC treatment (Figures 6J and 6K). In contrast, HSCs in a vit.A-free environment showed an impaired recovery of the quiescent state as shown by further reduced HSC frequencies and delayed return to G_0 (Figures 6J and 6K). Strikingly, HSC-Gpr^{pos} cells were not regenerated at this point after pIC-mediated activation in the absence of vitamin A (Figure 6L). Collectively, these data strongly suggest that vitamin A is required to maintain a potent HSC pool and to re-establish dHSCs during the recovery phase after pIC stimulation.

DISCUSSION

In agreement with their biological behavior, we now show by single-cell RNA-seq analysis that dHSCs harbor an extremely low overall biosynthetic activity. These biosynthetic processes gradually increase toward aHSCs indicating that the transition from dHSC to aHSCs can be better described as a continuously changing cellular state rather than the anticipated stepwise switch from one cell type to the next. The fact that numerous intermediate states are found may reflect the response to latent minor acute inflammatory events or result from stress responses that occurred in the past. For example, muscle stem cells show a transition from a G_0 to a G_{alert} state, which may represent a similar situation (Rodgers et al., 2014). The difference in the overall biosynthetic activity provides a valid explanation why dHSCs need ~11 hr longer to initiate their first productive cell cycle compared to aHSCs, which are themselves still in a non-cycling quiescent state. These data demonstrate the functional and molecular difference between: quiescent aHSCs (higher biosynthetic activity, cell-cycle primed/quick return into S-phase [G_0/G_1], RA-signature^{low}) and deeply dormant dHSCs (low biosynthetic activity, slow return into S-phase [G_0 only], RA-signature^{high}). The re-entry of dHSCs into the cell cycle is accompanied by the downregulation of p57 and the upregulation of the Cdk4/6 complex, both recently shown to play a crucial role in maintaining HSC quiescence and promoting initial HSC cell divisions, respectively (Laurenti et al., 2015; Matsumoto and Nakayama, 2013; Zou et al., 2011). The coordination between biosynthetic activity and cell-cycle-related processes with consequences on HSC function and differentiation has also recently been observed in other stem cell systems (Rodgers et al., 2014; Sanchez et al., 2016). For example, *Drosophila* germline stem cell differentiation relies on pathways promoting global protein synthesis (Sanchez et al., 2016), and overall protein production appears to be critical for progenitors (Signer et al., 2014). Low levels of Myc expression maintain naive embryonic stem cells (ESCs) and pre-implantation embryos in a dormant state of pluripotency (diapause) (Scognamiglio et al., 2016) likely mediated by the broad role of Myc in activating biosynthetic processes (Stine et al., 2015). In agreement, we find Myc expression to be very low in dHSCs and to steadily increase during the transition toward aHSCs and subsequently MPP1-4 (Cabezas-Wallscheid et al., 2014; Ehninger et al., 2014; Laurenti et al., 2008). In mice in which both Myc genes, c-Myc and N-Myc, have been deleted, only dHSCs survive, while all other hematopoietic cells are lost due to apoptosis, suggesting that only dHSCs are able to survive a completely Myc-deficient state (Laurenti et al., 2008). These

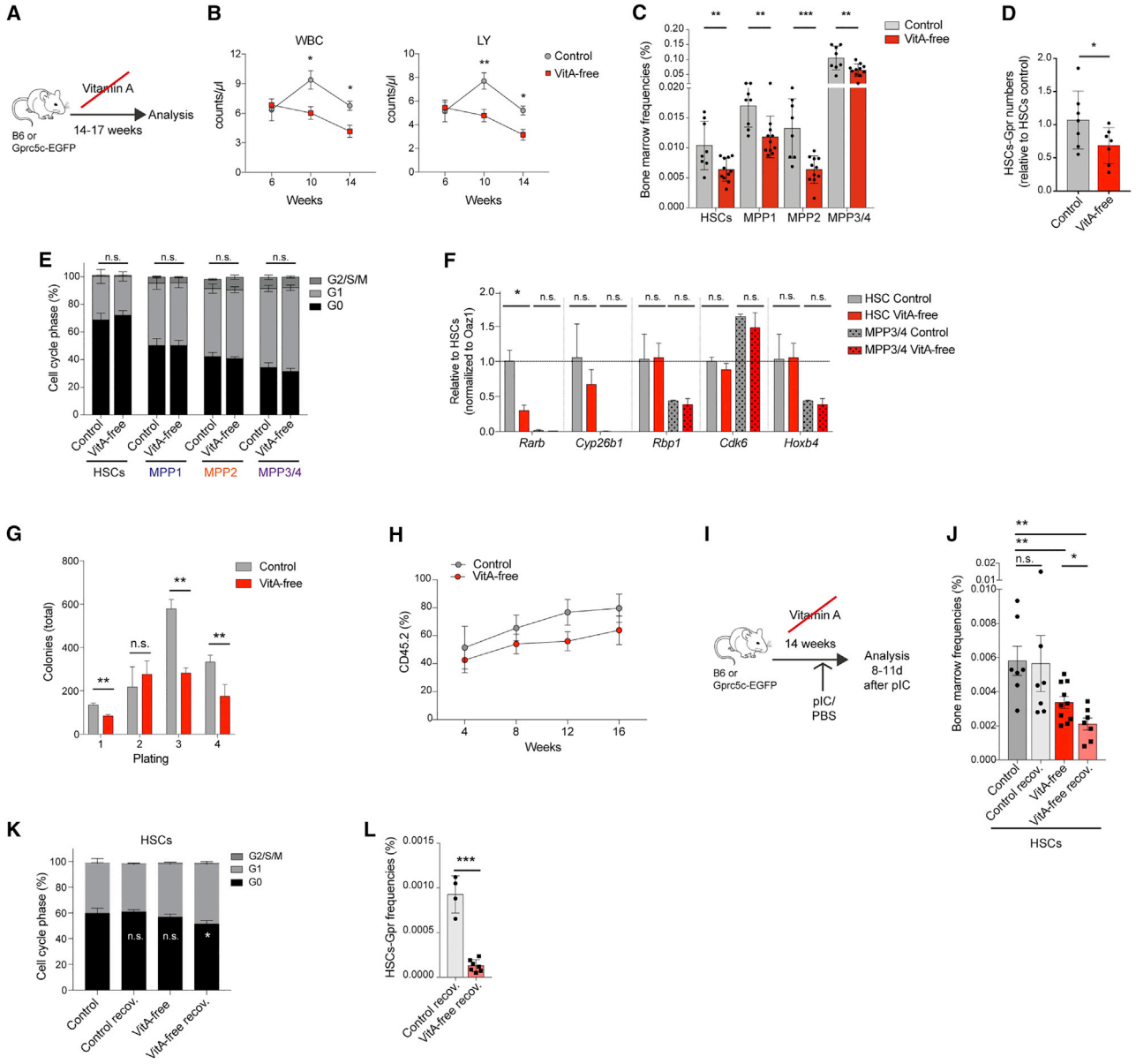

Figure 6. Consequences of a Vitamin A-free Diet for the Hematopoietic System

(A) Dietary workflow.

(B) Peripheral blood analysis over time. N = 6. PB, peripheral blood; WBC, white blood cells; LY, lymphocytes. Six to 14 weeks (w).

(C) HSCs, MPP1, MPP2, and MPP3/4 frequencies. Percentage of bone marrow HSC-MPPs are represented. N = 8–11.

(D) HSCs-Gpr numbers. Relative to control HSC-Gpr^{POS} and based on bone marrow cellularity. N = 7.

(E) Cell-cycle analysis. Relative percentage within each cell-cycle phase. N = 9–12.

(F) Molecular targets of vitamin A-free diet. qPCR of RA targets genes and cell-cycle regulators in HSCs and MPP3/4 upon 14 weeks vitamin A-free diet relative to HSCs. N = 3.

(G) Serial colony-forming unit assay (CFU). Total colonies are represented. N = 3–4.

(H) Transplantation experiments. CD45.2% outcome is represented. N = 4–5. One independent experiment.

(I and J) Reversibility of HSCs and MPP1 in a vitamin A-free environment. (I) Workflow. (J) HSC and MPP1 frequencies. Percentage of bone marrow HSCs and MPP1 are represented. N = 7–10.

(K) Cell-cycle analysis. Relative percentage within each cell-cycle phase. N = 6–10.

(L) Gpr-HSC frequencies. Percentage of bone marrow HSC-Gpr^{POS} are represented. N = 4–7. For all panels, Control, mice on normal diet; Control recov., mice on normal diet 8 to 11 days after pIC injection; VitA-free, mice on vitamin A-free diet for 14–17 weeks; VitA-free recov., mice on vitamin A-free diet for 14–17 weeks after 8–11 days after pIC injection; ±SEM is shown. *p <0.05; **p <0.01; ***p <0.001. n.s., not significant. N indicates biological replicates. For all experiments, greater than or equal to two independent experiments were performed unless otherwise indicated.

See also Figure S6.

data suggest that a threshold level of biosynthetic activity may be necessary for the initiation of differentiation of HSCs and possibly other stem cells, while low activity preserves stem cell potency and self-renewal potential.

Our transcriptome analysis revealed a highly significant enrichment of retinoic acid (RA)-induced target genes in dHSCs. Treatment of HSCs in vitro with the agonist all-*trans* retinoic acid (ATRA) induces cell-cycle arrest and inhibits proliferation, supporting previous observations (Jacobsen et al., 1994; Purton et al., 1999). Importantly, we now show by in vitro and in vivo analysis, that ATRA treatment preserves dHSCs and maintains critical properties of HSCs under stress conditions. These include maintenance of long-term self-renewal, low proliferation associated with decreased *Cdk6* levels, expression of key transcription factors (*Hoxb4*), reduced protein synthesis, and reactive oxygen species (ROS) generation as well as low Myc protein levels. However, ATRA treatment does not completely block HSC activation. Other pathways such as prostaglandin synthesis and regulation are also enriched in dHSCs and prostaglandin E2 (PGE2) has been shown to regulate HSC homeostasis (North et al., 2007). Thus RA and prostaglandin pathways may cooperate to maintain adult HSCs under various conditions, a possibility that can now be investigated at the molecular and functional level. ATRA protects HSCs from entering the cell cycle upon diverse stress stimuli (pIC, LPS, 5-FU) in vivo. This effect on HSCs is opposite to what occurs in more differentiated blood cells and certain leukemias, in which ATRA typically displays pro-differentiation effects (Collins, 2008; Masetti et al., 2012). This might be explained by cell-specific expression of the various RAR receptors. For example, ATRA plays a pro-differentiation role in acute promyelocytic leukemia harboring a promyelocytic leukemia (PML)-RARα translocation (Masetti et al., 2012). Our transcriptome data show a low expression of *Rarα* in the dHSC compartment. Indeed, PML leukemia-initiating cells (LIC) are established at the level of the granulocyte progenitor population with little resemblance to normal HSCs (Reinisch et al., 2016). Future studies should explore the exact mechanism of the distinct effect of RA signaling in dormant mouse and human HSCs and more mature cell types and acute myeloid leukemia (AML)-LICs.

Most of the studies on vitamin A deficit-associated immunodeficiency are dedicated to the impaired function of lymphocytes (Brown and Noelle, 2015; Mora et al., 2008). Our data obtained by analyzing mice fed with a vitamin A-deficient diet now extend the role of vitamin A-RA in the hematopoietic system to the regulation of HSCs in particular during inflammation-induced emergencies. These data were obtained using a systemic loss of vitamin A, and thus the effects could result from specific HSC autonomous and/or microenvironmental alterations. However, the following results argue that the vitamin A-deficient phenotype is caused, at least in part, by the impairment of the dHSC compartment: (1) dHSCs are characterized by a RA-signature^{high} phenotype, which is (2) specifically and reversibly changed during the activation process; (3) dHSC metabolize vitamin A in a cell-autonomous manner; (4) vitamin A-free HSCs have a decreased long-term self-renewal capacity (5) and are unable to re-establish a normal dHSC compartment upon stress. Together, these data argue that differential regulation of RA signaling controls the reversible balance between dormancy and self-renewal, most evident during stress response. The failure to return to the dormant state in the vitamin A-deficient microenvironment likely primes HSCs toward an irreversible differentiation trajectory with associated loss of self-renewal and HSC exhaustion. Collectively, our study highlights the implications and consequences that the absence of vitamin A in the diet or as dietary supplements may have on stem cell function and possibly associated diseases.

STAR★METHODS

Detailed methods are provided in the online version of this paper and include the following:

- KEY RESOURCES TABLE
- CONTACT FOR REAGENT AND RESOURCE SHARING
- EXPERIMENTAL MODEL AND SUBJECT DETAILS
  - Mice
- METHOD DETAILS
  - Cell suspensions and flow cytometry
  - Population RNA-seq
  - Single-cell RNA-seq
  - Immunofluorescence staining of Cdk6
  - Single-cell in vitro tracking of dHSC-aHSCs and HSCs-Gpr$^{pos/neg}$
  - Gprc5c-EGFP experiments
  - ATRA in vitro experiments
  - Gene expression analysis by qPCR
  - ATRA in vivo experiments
  - Vitamin A free diet
- QUANTIFICATION AND STATISTICAL ANALYSIS
- DATA AND SOFTWARE AVAILABILITY

SUPPLEMENTAL INFORMATION

Supplemental Information includes six figures and five tables and can be found with this article online at http://dx.doi.org/10.1016/j.cell.2017.04.018.

A video abstract is available at http://dx.doi.org/10.1016/j.cell.2017.04.018#mmc6.

AUTHOR CONTRIBUTIONS

Conceptualization, N.C.-W. and A.T.; Methodology, N.C.-W., F.B., P.S., D.K., L.L., F.B.T., D.P.-F., L.P.R., S.R., P.Z., A.P., K.S., R.S., S.A., C.M.F., M.F., M.T., D.V., P.C., and D.P.; Investigation, N.C.-W., F.B., P.S., D.K., S.R., V.B., O.S., and A.T.; Writing – Original Draft, N.C.-W. and A.T.; Writing – Review & Editing, N.C.-W., F.B., P.S., D.K., L.L., F.B.T., D.P.-F., L.P.R., S.R., K.S., R.S., S.A., C.M.F., H.G., T.S., T.P.D., M.A.R., O.S., and A.T.; Supervision, N.C.-W., O.S., and A.T.

ACKNOWLEDGMENTS

We thank M. Sohn and all technicians of the Trumpp laboratory for technical assistance; S. Schmitt, A. Atzberger, K. Hexel, M. Eich, G. de la Cruz, C. Felbinger from the DKFZ Flow Cytometry Core facility for their assistance; K. Reifenberg, M. Socher, A. Rathgeb and all members of the DKFZ Laboratory Animal Core Facility for excellent animal welfare and husbandry. We thank A. Hotz-Wagenblatt and the microarray unit of the DKFZ Genomics and Proteomics Core Facility for their assistance. We thank A. Wilson for critical reading of the manuscript. F.B. was supported by the UK Medical Research Council (MRC) via a Career Development Fellowship (MR/M01536X/1). This work was supported

by the FOR2033 and SFB873 funded by the Deutsche Forschungsgemeinschaft (DFG) and the Dietmar Hopp Foundation (all to A.T).

Received: February 20, 2017
Revised: April 6, 2017
Accepted: April 12, 2017
Published: May 4, 2017

REFERENCES

Acar, M., Kocherlakota, K.S., Murphy, M.M., Peyer, J.G., Oguro, H., Inra, C.N., Jaiyeola, C., Zhao, Z., Luby-Phelps, K., and Morrison, S.J. (2015). Deep imaging of bone marrow shows non-dividing stem cells are mainly perisinusoidal. Nature *526*, 126–130.

Anders, S., Pyl, P.T., and Huber, W. (2015). HTSeq–a Python framework to work with high-throughput sequencing data. Bioinformatics *31*, 166–169.

Angerer, P., Haghverdi, L., Buttner, M., Theis, F.J., Marr, C., and Buettner, F. (2015). destiny: diffusion maps for large-scale single-cell data in R. Bioinformatics *32*, 1241–1243.

Antonchuk, J., Sauvageau, G., and Humphries, R.K. (2001). HOXB4 overexpression mediates very rapid stem cell regeneration and competitive hematopoietic repopulation. Exp. Hematol. *29*, 1125–1134.

Ashburner, M., Ball, C.A., Blake, J.A., Botstein, D., Butler, H., Cherry, J.M., Davis, A.P., Dolinski, K., Dwight, S.S., Eppig, J.T., et al.; The Gene Ontology Consortium (2000). Gene ontology: tool for the unification of biology. Nat. Genet. *25*, 25–29.

Baldridge, M.T., King, K.Y., Boles, N.C., Weksberg, D.C., and Goodell, M.A. (2010). Quiescent haematopoietic stem cells are activated by IFN-gamma in response to chronic infection. Nature *465*, 793–797.

Balmer, J.E., and Blomhoff, R. (2002). Gene expression regulation by retinoic acid. J. Lipid Res. *43*, 1773–1808.

Beerman, I., Bhattacharya, D., Zandi, S., Sigvardsson, M., Weissman, I.L., Bryder, D., and Rossi, D.J. (2010). Functionally distinct hematopoietic stem cells modulate hematopoietic lineage potential during aging by a mechanism of clonal expansion. Proc. Natl. Acad. Sci. USA *107*, 5465–5470.

Bernitz, J.M., Kim, H.S., MacArthur, B., Sieburg, H., and Moore, K. (2016). Hematopoietic stem cells count and remember self-renewal divisions. Cell *167*, 1296–1309.

Brennecke, P., Anders, S., Kim, J.K., Kołodziejczyk, A.A., Zhang, X., Proserpio, V., Baying, B., Benes, V., Teichmann, S.A., Marioni, J.C., and Heisler, M.G. (2013). Accounting for technical noise in single-cell RNA-seq experiments. Nat. Methods *10*, 1093–1095.

Brown, C.C., and Noelle, R.J. (2015). Seeing through the dark: New insights into the immune regulatory functions of vitamin A. Eur. J. Immunol. *45*, 1287–1295.

Buettner, F., Natarajan, K.N., Casale, F.P., Proserpio, V., Scialdone, A., Theis, F.J., Teichmann, S.A., Marioni, J.C., and Stegle, O. (2015). Computational analysis of cell-to-cell heterogeneity in single-cell RNA-sequencing data reveals hidden subpopulations of cells. Nat. Biotechnol. *33*, 155–160.

Cabezas-Wallscheid, N., Klimmeck, D., Hansson, J., Lipka, D.B., Reyes, A., Wang, Q., Weichenhan, D., Lier, A., von Paleske, L., Renders, S., et al. (2014). Identification of regulatory networks in HSCs and their immediate progeny via integrated proteome, transcriptome, and DNA methylome analysis. Cell Stem Cell *15*, 507–522.

Chanda, B., Ditadi, A., Iscove, N.N., and Keller, G. (2013). Retinoic acid signaling is essential for embryonic hematopoietic stem cell development. Cell *155*, 215–227.

Chen, J.Y., Miyanishi, M., Wang, S.K., Yamazaki, S., Sinha, R., Kao, K.S., Seita, J., Sahoo, D., Nakauchi, H., and Weissman, I.L. (2016). Hoxb5 marks long-term haematopoietic stem cells and reveals a homogenous perivascular niche. Nature *530*, 223–227.

Chute, J.P., Muramoto, G.G., Whitesides, J., Colvin, M., Safi, R., Chao, N.J., and McDonnell, D.P. (2006). Inhibition of aldehyde dehydrogenase and retinoid signaling induces the expansion of human hematopoietic stem cells. Proc. Natl. Acad. Sci. USA *103*, 11707–11712.

Collins, S.J. (2008). Retinoic acid receptors, hematopoiesis and leukemogenesis. Curr. Opin. Hematol. *15*, 346–351.

Dobin, A., Davis, C.A., Schlesinger, F., Drenkow, J., Zaleski, C., Jha, S., Batut, P., Chaisson, M., and Gingeras, T.R. (2013). STAR: ultrafast universal RNA-seq aligner. Bioinformatics *29*, 15–21.

Ehninger, A., Boch, T., Uckelmann, H., Essers, M.A., Müdder, K., Sleckman, B.P., and Trumpp, A. (2014). Posttranscriptional regulation of c-Myc expression in adult murine HSCs during homeostasis and interferon-α-induced stress response. Blood *123*, 3909–3913.

Essers, M.A., Offner, S., Blanco-Bose, W.E., Waibler, Z., Kalinke, U., Duchosal, M.A., and Trumpp, A. (2009). IFNalpha activates dormant haematopoietic stem cells in vivo. Nature *458*, 904–908.

Foudi, A., Hochedlinger, K., Van Buren, D., Schindler, J.W., Jaenisch, R., Carey, V., and Hock, H. (2009). Analysis of histone 2B-GFP retention reveals slowly cycling hematopoietic stem cells. Nat. Biotechnol. *27*, 84–90.

Fujikawa, Y., Roma, L.P., Sobotta, M.C., Rose, A.J., Diaz, M.B., Locatelli, G., Breckwoldt, M.O., Misgeld, T., Kerschensteiner, M., Herzig, S., et al. (2016). Mouse redox histology using genetically encoded probes. Sci. Signal. *9*, rs1.

Gazit, R., Mandal, P.K., Ebina, W., Ben-Zvi, A., Nombela-Arrieta, C., Silberstein, L.E., and Rossi, D.J. (2014a). Fgd5 identifies hematopoietic stem cells in the murine bone marrow. J. Exp. Med. *211*, 1315–1331.

Ghiaur, G., Yegnasubramanian, S., Perkins, B., Gucwa, J.L., Gerber, J.M., and Jones, R.J. (2013). Regulation of human hematopoietic stem cell self-renewal by the microenvironment's control of retinoic acid signaling. Proc. Natl. Acad. Sci. USA *110*, 16121–16126.

Gong, S., Zheng, C., Doughty, M.L., Losos, K., Didkovsky, N., Schambra, U.B., Nowak, N.J., Joyner, A., Leblanc, G., Hatten, M.E., and Heintz, N. (2003). A gene expression atlas of the central nervous system based on bacterial artificial chromosomes. Nature *425*, 917–925.

Graf, T., and Enver, T. (2009). Forcing cells to change lineages. Nature *462*, 587–594.

Haetscher, N., Feuermann, Y., Wingert, S., Rehage, M., Thalheimer, F.B., Weiser, C., Bohnenberger, H., Jung, K., Schroeder, T., Serve, H., et al. (2015). STAT5-regulated microRNA-193b controls haematopoietic stem and progenitor cell expansion by modulating cytokine receptor signalling. Nat. Commun. *6*, 8928.

Haghverdi, L., Buettner, F., and Theis, F.J. (2015). Diffusion maps for high-dimensional single-cell analysis of differentiation data. Bioinformatics *31*, 2989–2998.

Haghverdi, L., Büttner, M., Wolf, F.A., Buettner, F., and Theis, F.J. (2016). Diffusion pseudotime robustly reconstructs lineage branching. Nat. Methods *13*, 845–848.

Huang, C.Y., Bredemeyer, A.L., Walker, L.M., Bassing, C.H., and Sleckman, B.P. (2008). Dynamic regulation of c-Myc proto-oncogene expression during lymphocyte development revealed by a GFP-c-Myc knock-in mouse. Eur. J. Immunol. *38*, 342–349.

Jacobsen, S.E., Fahlman, C., Blomhoff, H.K., Okkenhaug, C., Rusten, L.S., and Smeland, E.B. (1994). All-trans- and 9-cis-retinoic acid: potent direct inhibitors of primitive murine hematopoietic progenitors in vitro. J. Exp. Med. *179*, 1665–1670.

Klimmeck, D., Cabezas-Wallscheid, N., Reyes, A., von Paleske, L., Renders, S., Hansson, J., Krijgsveld, J., Huber, W., and Trumpp, A. (2014). Transcriptome-wide profiling and posttranscriptional analysis of hematopoietic stem/progenitor cell differentiation toward myeloid commitment. Stem Cell Reports *3*, 858–875.

Kutmon, M., Riutta, A., Nunes, N., Hanspers, K., Willighagen, E.L., Bohler, A., Mélius, J., Waagmeester, A., Sinha, S.R., Miller, R., et al. (2016). WikiPathways: capturing the full diversity of pathway knowledge. Nucleic Acids Res. *44*(D1), D488–D494.

Laurenti, E., Varnum-Finney, B., Wilson, A., Ferrero, I., Blanco-Bose, W.E., Ehninger, A., Knoepfler, P.S., Cheng, P.F., MacDonald, H.R., Eisenman, R.N., et al. (2008). Hematopoietic stem cell function and survival depend on c-Myc and N-Myc activity. Cell Stem Cell *3*, 611–624.

Laurenti, E., Frelin, C., Xie, S., Ferrari, R., Dunant, C.F., Zandi, S., Neumann, A., Plumb, I., Doulatov, S., Chen, J., et al. (2015). CDK6 levels regulate quiescence exit in human hematopoietic stem cells. Cell Stem Cell *16*, 302–313.

Lipka, D.B., Wang, Q., Cabezas-Wallscheid, N., Klimmeck, D., Weichenhan, D., Herrmann, C., Lier, A., Brocks, D., von Paleske, L., Renders, S., et al. (2014). Identification of DNA methylation changes at cis-regulatory elements during early steps of HSC differentiation using tagmentation-based whole genome bisulfite sequencing. Cell Cycle *13*, 3476–3487.

Liu, J., Xu, Y., Stoleru, D., and Salic, A. (2012). Imaging protein synthesis in cells and tissues with an alkyne analog of puromycin. Proc. Natl. Acad. Sci. USA *109*, 413–418.

Love, M.I., Huber, W., and Anders, S. (2014). Moderated estimation of fold change and dispersion for RNA-seq data with DESeq2. Genome Biol. *15*, 550.

Ludin, A., Gur-Cohen, S., Golan, K., Kaufmann, K.B., Itkin, T., Medaglia, C., Lu, X.J., Ledergor, G., Kollet, O., and Lapidot, T. (2014). Reactive oxygen species regulate hematopoietic stem cell self-renewal, migration and development, as well as their bone marrow microenvironment. Antioxid. Redox Signal. *21*, 1605–1619.

Masetti, R., Vendemini, F., Zama, D., Biagi, C., Gasperini, P., and Pession, A. (2012). All-trans retinoic acid in the treatment of pediatric acute promyelocytic leukemia. Expert Rev. Anticancer Ther. *12*, 1191–1204.

Matsumoto, A., and Nakayama, K.I. (2013). Role of key regulators of the cell cycle in maintenance of hematopoietic stem cells. Biochim. Biophys. Acta *1830*, 2335–2344.

Meyer, A.J., and Dick, T.P. (2010). Fluorescent protein-based redox probes. Antioxid. Redox Signal. *13*, 621–650.

Mora, J.R., Iwata, M., and von Andrian, U.H. (2008). Vitamin effects on the immune system: vitamins A and D take centre stage. Nat. Rev. Immunol. *8*, 685–698.

Morita, Y., Ema, H., and Nakauchi, H. (2010). Heterogeneity and hierarchy within the most primitive hematopoietic stem cell compartment. J. Exp. Med. *207*, 1173–1182.

North, T.E., Goessling, W., Walkley, C.R., Lengerke, C., Kopani, K.R., Lord, A.M., Weber, G.J., Bowman, T.V., Jang, I.H., Grosser, T., et al. (2007). Prostaglandin E2 regulates vertebrate haematopoietic stem cell homeostasis. Nature *447*, 1007–1011.

Pierce, K.L., Premont, R.T., and Lefkowitz, R.J. (2002). Seven-transmembrane receptors. Nat. Rev. Mol. Cell Biol. *3*, 639–650.

Purton, L.E., Bernstein, I.D., and Collins, S.J. (1999). All-trans retinoic acid delays the differentiation of primitive hematopoietic precursors (lin-c-kit+Sca-1(+)) while enhancing the terminal maturation of committed granulocyte/monocyte progenitors. Blood *94*, 483–495.

Purton, L.E., Bernstein, I.D., and Collins, S.J. (2000). All-trans retinoic acid enhances the long-term repopulating activity of cultured hematopoietic stem cells. Blood *95*, 470–477.

Qiu, J., Papatsenko, D., Niu, X., Schaniel, C., and Moore, K. (2014). Divisional history and hematopoietic stem cell function during homeostasis. Stem Cell Reports *2*, 473–490.

Reinisch, A., Thomas, D., Corces, M.R., Zhang, X., Gratzinger, D., Hong, W.J., Schallmoser, K., Strunk, D., and Majeti, R. (2016). A humanized bone marrow ossicle xenotransplantation model enables improved engraftment of healthy and leukemic human hematopoietic cells. Nat. Med. *22*, 812–821.

Rieger, M.A., Hoppe, P.S., Smejkal, B.M., Eitelhuber, A.C., and Schroeder, T. (2009). Hematopoietic cytokines can instruct lineage choice. Science *325*, 217–218.

Robbins, M.J., Michalovich, D., Hill, J., Calver, A.R., Medhurst, A.D., Gloger, I., Sims, M., Middlemiss, D.N., and Pangalos, M.N. (2000). Molecular cloning and characterization of two novel retinoic acid-inducible orphan G-protein-coupled receptors (GPRC5B and GPRC5C). Genomics *67*, 8–18.

Rodgers, J.T., King, K.Y., Brett, J.O., Cromie, M.J., Charville, G.W., Maguire, K.K., Brunson, C., Mastey, N., Liu, L., Tsai, C.R., et al. (2014). mTORC1 controls the adaptive transition of quiescent stem cells from G0 to G(Alert). Nature *510*, 393–396.

Sanchez, C.G., Teixeira, F.K., Czech, B., Preall, J.B., Zamparini, A.L., Seifert, J.R., Malone, C.D., Hannon, G.J., and Lehmann, R. (2016). Regulation of ribosome biogenesis and protein synthesis controls germline stem cell differentiation. Cell Stem Cell *18*, 276–290.

Sano, T., Kim, Y.J., Oshima, E., Shimizu, C., Kiyonari, H., Abe, T., Higashi, H., Yamada, K., and Hirabayashi, Y. (2011). Comparative characterization of GPRC5B and GPRC5CLacZ knockin mice; behavioral abnormalities in GPRC5B-deficient mice. Biochem. Biophys. Res. Commun. *412*, 460–465.

Scialdone, A., Natarajan, K.N., Saraiva, L.R., Proserpio, V., Teichmann, S.A., Stegle, O., Marioni, J.C., and Buettner, F. (2015). Computational assignment of cell-cycle stage from single-cell transcriptome data. Methods *85*, 54–61.

Scognamiglio, R., Cabezas-Wallscheid, N., Thier, M.C., Altamura, S., Reyes, A., Prendergast, A.M., Baumgärtner, D., Carnevalli, L.S., Atzberger, A., Haas, S., et al. (2016). Myc depletion induces a pluripotent dormant state mimicking diapause. Cell *164*, 668–680.

Seita, J., and Weissman, I.L. (2010). Hematopoietic stem cell: self-renewal versus differentiation. Wiley Interdiscip. Rev. Syst. Biol. Med. *2*, 640–653.

Signer, R.A., Magee, J.A., Salic, A., and Morrison, S.J. (2014). Haematopoietic stem cells require a highly regulated protein synthesis rate. Nature *509*, 49–54.

Stine, Z.E., Walton, Z.E., Altman, B.J., Hsieh, A.L., and Dang, C.V. (2015). MYC, metabolism, and cancer. Cancer Discov. *5*, 1024–1039.

Suda, T., Takubo, K., and Semenza, G.L. (2011). Metabolic regulation of hematopoietic stem cells in the hypoxic niche. Cell Stem Cell *9*, 298–310.

Takizawa, H., Regoes, R.R., Boddupalli, C.S., Bonhoeffer, S., and Manz, M.G. (2011). Dynamic variation in cycling of hematopoietic stem cells in steady state and inflammation. J. Exp. Med. *208*, 273–284.

Tang, X.H., and Gudas, L.J. (2011). Retinoids, retinoic acid receptors, and cancer. Annu. Rev. Pathol. *6*, 345–364.

Tesio, M., Tang, Y., Müdder, K., Saini, M., von Paleske, L., Macintyre, E., Pasparakis, M., Waisman, A., and Trumpp, A. (2015). Hematopoietic stem cell quiescence and function are controlled by the CYLD-TRAF2-p38MAPK pathway. J. Exp. Med. *212*, 525–538.

Thalheimer, F.B., Wingert, S., De Giacomo, P., Haetscher, N., Rehage, M., Brill, B., Theis, F.J., Hennighausen, L., Schroeder, T., and Rieger, M.A. (2014). Cytokine-regulated GADD45G induces differentiation and lineage selection in hematopoietic stem cells. Stem Cell Reports *3*, 34–43.

Till, J.E., and McCulloch, E.A. (1961). A direct measurement of the radiation sensitivity of normal mouse bone marrow cells. Radiat. Res. *14*, 213–222.

Trapnell, C., Cacchiarelli, D., Grimsby, J., Pokharel, P., Li, S., Morse, M., Lennon, N.J., Livak, K.J., Mikkelsen, T.S., and Rinn, J.L. (2014). The dynamics and regulators of cell fate decisions are revealed by pseudotemporal ordering of single cells. Nat. Biotechnol. *32*, 381–386.

van der Maaten, L., and Hinton, G. (2008). Visualizing data using t-SNE. J. Mach. Learn. Res. *9*, 2579–2605.

van der Wath, R.C., Wilson, A., Laurenti, E., Trumpp, A., and Liò, P. (2009). Estimating dormant and active hematopoietic stem cell kinetics through extensive modeling of bromodeoxyuridine label-retaining cell dynamics. PLoS ONE *4*, e6972.

Venezia, T.A., Merchant, A.A., Ramos, C.A., Whitehouse, N.L., Young, A.S., Shaw, C.A., and Goodell, M.A. (2004). Molecular signatures of proliferation and quiescence in hematopoietic stem cells. PLoS Biol. *2*, e301.

Wagner, K. (1940). Die experimentelle Avitaminose A beim Menschen. Hoppe Seylers Z. Physiol. Chem. *264*, 153–189.

Walter, D., Lier, A., Geiselhart, A., Thalheimer, F.B., Huntscha, S., Sobotta, M.C., Moehrle, B., Brocks, D., Bayindir, I., Kaschutnig, P., et al. (2015). Exit

from dormancy provokes DNA-damage-induced attrition in haematopoietic stem cells. Nature *520*, 549–552.

Wilson, A., Laurenti, E., Oser, G., van der Wath, R.C., Blanco-Bose, W., Jaworski, M., Offner, S., Dunant, C.F., Eshkind, L., Bockamp, E., et al. (2008). Hematopoietic stem cells reversibly switch from dormancy to self-renewal during homeostasis and repair. Cell *135*, 1118–1129.

Wilson, N.K., Kent, D.G., Buettner, F., Shehata, M., Macaulay, I.C., Calero-Nieto, F.J., Sánchez Castillo, M., Oedekoven, C.A., Diamanti, E., Schulte, R., et al. (2015). Combined single-cell functional and gene expression analysis resolves heterogeneity within stem cell populations. Cell Stem Cell *16*, 712–724.

Wu, D., and Smyth, G.K. (2012). Camera: a competitive gene set test accounting for inter-gene correlation. Nucleic Acids Res. *40*, e133.

Zirath, H., Frenzel, A., Oliynyk, G., Segerström, L., Westermark, U.K., Larsson, K., Munksgaard Persson, M., Hultenby, K., Lehtiö, J., Einvik, C., et al. (2013). MYC inhibition induces metabolic changes leading to accumulation of lipid droplets in tumor cells. Proc. Natl. Acad. Sci. USA *110*, 10258–10263.

Zou, P., Yoshihara, H., Hosokawa, K., Tai, I., Shinmyozu, K., Tsukahara, F., Maru, Y., Nakayama, K., Nakayama, K.I., and Suda, T. (2011). p57(Kip2) and p27(Kip1) cooperate to maintain hematopoietic stem cell quiescence through interactions with Hsc70. Cell Stem Cell *9*, 247–261.

STAR★METHODS

KEY RESOURCES TABLE

REAGENT or RESOURCE	SOURCE	IDENTIFIER
Antibodies		
anti-alpha tubulin	AbCam	ab6160
anti-Cdk6	Invitrogen	ahz0232
anti-rat DyLight488-conjugated antibody	Jackson ImmunoResearch	Cat#211-482-171
anti-mouse Cy3-conjugated antibody	Jackson ImmunoResearch	Cat#715-165-150
anti-mouse CD4-PE-Cy7 (clone: GK1.5)	eBioscience	25-0041
anti-mouse CD8a-PE-Cy7 (clone: 53-6.7)	eBioscience	25-0081
anti-mouse CD11b-PE-Cy7 (clone: M1/70)	eBioscience	25-0112
anti-mouse B220-PE-Cy7 (clone: RA3-6B2)	eBioscience	25-0452
anti-mouse Ter119-PE-Cy7 (clone: TER-119)	eBioscience	25-5921
anti-mouse Gr1-PE-Cy7 (clone: RB6-8C5)	eBioscience	25-5931
anti-mouse CD117(c-Kit)-APC-eFluor780 (clone: 2B8)	eBioscience	47-1171
anti-mouse Ly-6A/E(Sca-1)-APC (clone: D7)	eBioscience	17-5981
anti-mouse CD150-PE-Cy5 (clone: TC15-12F12.2)	BioLegend	115912
anti-mouse CD48-PB (clone: HM48-1)	BioLegend	103418
anti-mouse CD34-AF700 (clone: RAM34)	eBioscience	56-0341
anti-human Ki67-AF647 (clone: B56)	BD Biosciences	558615
anti-mouse CD4-biotin (clone: GK1.5)	eBioscience	13-0041
anti-mouse CD8a-biotin (clone: 53-6.7)	eBioscience	13-0081
anti-mouse CD11b-biotin (clone: M1/70)	eBioscience	13-0112
anti-mouse B220-biotin (clone: RA3-6B2	eBioscience	13-0452
anti-mouse Ter119-biotin (clone: TER-119)	eBioscience	13-5921
anti-mouse Gr1-biotin (clone: RB6-8C5)	eBioscience	13-5931
anti-mouse CD71-PE (clone: R17217)	eBioscience	12-0711
anti-mouse IgM-PE-Cy5 (clone: II/41)	eBioscience	15-5790
Chemicals, Peptides, and Recombinant Proteins		
5-Fluororacil (5-FU)	Sigma-Aldrich	F6627
7-Aminoactinomycin D (7AAD)	LifeTechnologies	A1310
ACK Lysing Buffer	Lonza	Cat#10-548E
Alexa647-azide	LifeTechnologies	A10277
Antimycin A from *Streptomyces* sp.	Sigma-Aldrich	A8674
C1 Single-Cell Reagent Kit for mRNA Seq	Fluidigm	Cat# 100-6201
Diamide	Sigma-Aldrich	D3648-1G
Donkey Serum	Sigma-Aldrich	D9663
Doxycycline (Dox)	Sigma-Aldrich	Cat#D9891
Dithiothreitol (DTT)	Applichem	A1101
ERCC RNA Spike-In Mix	Thermo fisher	Cat# 4456740
Hoechst 33342	Invitrogen	H3570
LPS from *Escherichia coli*	Sigma-Aldrich	L2360
MethoCult M3434	StemCell Technologies	Cat# 03434
Myc inhibitor 10058-F4	Calbiochem, Merck Millipore	Cat#475956
O-propargyl-puromycin (OP-Puro)	Jena Biosciences	NU-931-05
Poly(I:C) HMW	InvivoGen	tlrl-pic-5
ProLong Gold Antifade Reagent with DAPI	Invitrogen	P36931

(*Continued on next page*)

Continued

REAGENT or RESOURCE	SOURCE	IDENTIFIER
Recombinant Human Flt3	PeproTech	Cat#300-19
Recombinant Murine Stem Cell Factor	PeproTech	Cat#250-03
Recombinant Murine Thrombopoietin	PeproTech	Cat#315-14
Retinoic Acid	Sigma-Aldrich	R2625
Retinol	Sigma-Aldrich	R7632
Saponin	Sigma-Aldrich	Cat#4703
StemPro-34 SFM (1X)	LifeTechnologies	Cat#10639011
Triton X-100	Sigma-Aldrich	T8787
Critical Commercial Assays		
BD Cytofix/Cytoperm Kit	Becton Dickinson	Cat#554722
GeneChip Mouse Gene 2.0 ST Array	Affymetrix	Cat#902463
Click-iT Cell Reaction Buffer Kit	LifeTechnologies	Cat#10269
C1 Auto-Prep 5-10μM Integrated Fluidic Chip (IFC)	Fluidigm	Cat#100-5759
PE Active Caspase-3 Apoptosis Kit	Becton Dickinson	Cat#550914
Dynabeads Untouched Mouse CD4 Kit	LifeTechnologies	Cat#11415D
FastSYBR Green Master Mix	Applied Biosystems	Cat#4385612
Nextera XT DNA Sample Preparation Kits	Illumina	Cat#1502354
OneComp eBeads	eBioscience	Cat#01-1111-41
PicoPure RNA Isolation Kit	Applied Biosystems	# KIT0202
FC-131-1096 SMARTer Ultra Low RNA Kit for the Fluidigm C1	ClonTech Laboratories	Cat#634832
SMARTer Ultra Low RNA Kit for Illumina Sequencing	ClonTech Laboratories	Cat#634936
SuperScript VILO cDNA Synthesis Kit	Invitrogen	Cat#11754050
Deposited Data		
Population RNA-seq data	This paper	ArrayExpress: E-MTAB-4549; http://www.ebi.ac.uk/arrayexpress/; E-MTAB-4549
Single-cell RNA-seq data	This paper	ArrayExpress: E-MTAB-4547; http://www.ebi.ac.uk/arrayexpress/; E-MTAB-4547
Microarray data	This paper	GEO: GSE87814; https://www.ncbi.nlm.nih.gov/gds; GSE87814
Experimental Models: Organisms/Strains		
Mouse: SCL-tTA;H2B-GFP	(Wilson et al., 2008)	N/A
Mouse: tg(Gprc5c-EGFP)JU90Gsat	(Gong et al., 2003)	N/A
Mouse: Myc-eGFP	(Huang et al., 2008)	N/A
Mouse: Mito-roGFP2-Orp1	(Fujikawa et al., 2016)	N/A
Mouse: C57BL/6J	Harlan Laboratories	ID:057
Mouse: Gprc5c-KO	(Sano et al., 2011)	N/A
Oligonucleotides		
See Table S5 for list of primers.		
Software and Algorithms		
Affymetrix Gene Chip Operating Software (GCOS)	Affymetrix	http://www.affymetrix.com/browse/products.jsp?productId=131429&navMode=34000&navAction=jump&aId=productsNav
CAMERA	(Wu and Smyth, 2012)	http://www.rdocumentation.org/packages/edgeR/versions/3.14.0

(*Continued on next page*)

Continued

REAGENT or RESOURCE	SOURCE	IDENTIFIER
cyclone	(Scialdone et al., 2015)	https://github.com/PMBio/cyclone
Data analysis (FACS)	FlowJo 10, TreeStar	https://www.flowjo.com/solutions/flowjo/downloads
Data analysis	Graph Pad Prism 6, GraphPad	https://www.graphpad.com/scientific-software/prism/
DESeq2	(Love et al., 2014)	https://bioconductor.org/packages/release/bioc/html/DESeq2.html
destiny	(Angerer et al., 2015)	https://www.bioconductor.org/packages/devel/bioc/html/destiny.html
gplots	R package	https://cran.r-project.org/web/packages/gplots/index.html.
HTSeq	(Anders et al., 2015)	https://pypi.python.org/pypi/HTSeq/0.6.1
scLVM	(Buettner et al., 2015)	https://github.com/PMBio/scLVM
oligo package	Bioconductor	http://bioconductor.org/packages/release/bioc/html/oligo.html
STAR	(Dobin et al., 2013)	https://github.com/alexdobin/STAR/releases/tag/STAR_2.4.0h
topGO	Bioconductor	https://bioconductor.org/packages/release/bioc/html/topGO.html
t-SNE	(van der Maaten and Hinton, 2008)	https://cran.r-project.org/web/packages/Rtsne/index.html
ViAA 7 Software v1.1	Applied Biosystems	https://www.thermofisher.com/us/en/home/technical-resources/software-downloads/applied-biosystems-viia-7-real-time-pcr-system.html.
WikiPathways	(Kutmon et al., 2016)	http://www.wikipathways.org/index.php/WikiPathways

CONTACT FOR REAGENT AND RESOURCE SHARING

Further information and requests for resources and reagents should be directed to and will be fulfilled by the Lead Contact, Andreas Trumpp (a.trumpp@dkfz.de). Certain materials are shared with research organizations for research and educational purposes only under an MTA to be discussed in good faith with the recipient.

EXPERIMENTAL MODEL AND SUBJECT DETAILS

Mice

The transgenic mouse line, SCL-tTA; H2B-GFP, which expresses the fusion protein histone H2B-GFP under the tetracycline-responsive regulatory element and the tTA-S2 transactivator from the endogenous SCL locus (Wilson et al., 2008). Doxycycline was supplemented in drinking water of 8-12 weeks old mice for 150 days as previously described (Wilson et al., 2008). Backcrossed to C57BL/6J. *Gprc5c-EGFP*. Tg(Gprc5c-EGFP)JU90Gsat. EGFP gene was inserted into a BAC clone at the initiating ATG codon of the first coding exon of the Gprc5c gene and this BAC clone was subsequently used to generate transgenic reporter mice (Gong et al., 2003). Backcrossed to C57BL/6J. > 20-week old mice were used through the study (similar age as SCL-tTA;H2B-GFP at the time of analysis = 8-12 weeks + 150 days DOX) unless not otherwise specified. *Myc-eGFP*. *Knockin* mouse model that expresses a fusion protein of c-Myc and eGFP. c-MyceGFP/eGFP (Huang et al., 2008). 8-12 weeks old mice were used through the study. *Mito-roGFP2-Orp1*. Mito-roGFP2-Orp1 expressing mice were generated as detailed in (Fujikawa et al., 2016). 8-12 weeks old mice were used through the study. *C57BL/6J*. 8- to 20-week-old (CD45.2, CD45.1 or CD45.2/CD45.1) mice were either purchased from Harlan Laboratories (the Netherlands) or breed in-house. *Gprc5c-KO*. 8- to 12-week-old mice were used. Knockout mice were generated and described by (Sano et al., 2011). All mice were bred in-house in the animal facility at the DKFZ under specific pathogen free (SPF) conditions in individually ventilated cages (IVC). According to German guidelines, mice were euthanized by cervical dislocation. Animal procedures were performed according to protocols approved by the German authorities, Regierungspräsidium Karlsruhe (Nr. Z110/02, DKFZ 299, G232-12, G94-11 and G162-15).

METHOD DETAILS

Cell suspensions and flow cytometry

Mouse bone marrow (BM) cells were isolated, and dHSC, aHSC and MPP1 progenitors defined by immunophenotype (Lineage$^-$ Sca1$^+$ Kit$^+$ CD150+ CD48- CD34+/−) and label-retention (for SCL-tTA;H2B-GFP) or EGFP signal (for Gprc5c-EGFP), or LSK were purified by FACS and subsequently subjected to population RNA-seq, in vitro tracking, CFU analysis or reconstitution assays. Briefly, BM was isolated from pooled femora, tibiae, ilia and vertebrae by gentle crushing in PBS 2%FCS using a mortar and pistil. Lysis of erythrocytes was performed using ACK Lysing Buffer (Thermo Fisher Scientific). To deplete lineage-positive cells we used the Dynabeads Untouched Mouse CD4 Cells Kit (Invitrogen). Briefly, total BM was stained for 30 min with a 1:5 dilution of the Lineage Cocktail provided in the Dynabeads Untouched Mouse CD4 Cells Kit (Invitrogen). Labeled cells were then incubated for 20 min with 1.5 mL/mouse of washed polyclonal sheep anti-rat IgG coated Dynabeads provided in the Kit. Cells were depleted using a magnet, enriching for the lineage-negative (Lineage$^-$) cell fraction. To purify hematopoietic stem cells, the Lineage$^-$ fraction was stained for 30 min using the following monoclonal antibodies: anti-lineage [anti-CD4 (clone GK1.5), anti-CD8a (53-6.7), anti-CD11b (M1/70), anti-B220 (RA3-6B2), anti-GR1 (RB6-8C5) and anti-TER119 (Ter-119)] all PE-Cy7; anti-CD117/c-Kit (2B8)-APC-eFl780; anti-Ly6a/Sca-1 (D7)-APC; anti-CD34 (RAM34)-Alexa700; anti-CD150 (TC15-12F12.2)-PE-Cy5; anti-CD48 (HM48-1)-PB. Monoclonal antibody conjugates were purchased from eBioscience or BioLegend. Cell sorting was then performed on a FACS Aria I, II and III (Becton Dickinson). Sorted cells were collected into ice-cold PBS (reconstitution assays), Complete Stem Cell Medium (specified elsewhere) for CFUs, SiC imaging and in vitro tracking experiments, RNA lysis buffer (ARCTURUS PicoPure RNA Isolation Kit (Life Technologies, Invitrogen)) for population RNA-seq, qPCR and stored at −80°C. Sort purity was > 95% in all cases.

Population RNA-seq

Generation

Population RNA-seq data were generated as previously described (Cabezas-Wallscheid et al., 2014; Klimmeck et al., 2014). Briefly, total RNA isolation was performed using ARCTURUS PicoPure RNA Isolation Kit (Life Technologies, Invitrogen) according to the manufacturer's instructions. Total RNA was used for quality controls and for normalization of starting material. cDNA-libraries were generated with 1 ng of total RNA for dHSCs, aHSCs and MPP1 using the SMARTer Ultra Low RNA Kit for Illumina Sequencing (ClonTech) according to the manufacturer's indications. Sequencing was performed with the HiSeq2000 device (Illumina) using one sample per lane, resulting in between 272,204,749 and 457,840,113 reads per sample. Workflow and quality controls (QCs) summarized in Figures S1A and S1B.

Low level processing

Sequenced read fragments were mapped to the mouse reference genome GRCm38 (ENSEMBL release 69) using STAR (STAR_2.4.0h) (Dobin et al., 2013). Expression counts estimates were generated using HTSeq (0.6.1) (Anders et al., 2015). DESeq2 (Love et al., 2014) was used to test for differential expression; results were considered significant at an FDR < 0.1.

Downstream analysis

PCA visualization was performed based on variance stabilized read counts using the DESeq2 package (Love et al., 2014). Differential expression analyses were performed using a Wald test to test for significance of coefficients in a Negative Binomial GLM with the DESeq2 package. We used CAMERA (Wu and Smyth, 2012) to test whether a set of genes annotated to pathways form WikiPathways (Kutmon et al., 2016) was highly ranked relative to other genes in terms of differential expression (Figures 1F and 1G; FDR < 0.1).

Single-cell RNA-seq

Generation

Capture of single cells were performed using the C1 Auto-Prep 5-10μM Integrated Fluidic Chip (IFC) (Fluidigm) then imaged and annotated under bright field light microscopy using 20x objective to confirm single-cell capture. Cells captured alongside debris, doublet cells and dead cells were flagged for exclusion in downstream analysis. Subsequent reverse transcription and amplification of cDNA was performed on-chip using the Smarter Ultra Low RNA Kit (ClonTech) chemistry according to Fluidigm C1 protocol. Library prep for Illumina sequencing was carried out only on single-cells confirmed by microscopy using Nextera XT DNA Sample preparation kits (Illumina) 1.25 μL cDNA for each cell, tagmentation has been done according to the Fluidigm C1 protocol. Each Fluidigm IFC capture was pooled and sequenced over 2 lanes per pool on Illumina HiSeq 2500. ERCC (External RNA Controls Consortium) spike-in dilution 1:4000. Workflow and quality controls (QCs) summarized in Figure S2A.

Low level processing

Raw sequencing reads were mapped with STAR (STAR_2.4.0h) (Dobin et al., 2013), using a custom reference containing both the reference mouse genome (GRCm38) along with ERCC sequences. Expression counts estimates were generated using HTSeq (0.6.1) (Anders et al., 2015).

Following the counting of mapped reads, we imposed additional quality control criteria to identify and remove low quality cells. Cells that did not pass all of the six following criteria were removed from the analysis:

- Total number of reads > 50,000,
- Percentage of reads mapping to known exons > 20%,

- Number of genes detected (at least one mapped read) > 1,000
- Percentage of reads mapping to ERCC < 30%
- Percentage of mitochondrial reads < 15%
- Percentage of low alignment quality reads based on HTSeq < 10%

A set of 319 out of 384 cells passed all criteria, consisting of 173 HSCs and 146 dHSCs. We next performed size factor normalization using a standard DESeq size factor estimated from reads mapped to endogenous genes (Figure S2). To assess the effect of technical noise, we first used a log-linear fit to capture the relationship between mean and squared coefficient of variation (CV) of the log-transformed, size-factor normalized data (Brennecke et al., 2013). We then considered genes with a squared CV greater than the estimated squared baseline CV as variable beyond technical noise. This filter for highly variable genes resulted in 4,707 genes, which were used for all downstream analyses.

Quality controls

To account for possible batch effects, we next applied scLVM (Buettner et al., 2015) (https://github.com/PMBio/scLVM) to regress out such batch effects, controlling for experimental design (cell type). Covariance matrices for batch as well as cell type were modeled using a delta kernel (dummy coding the batches) and treated as random effects. As quality control that batch effects were accounted for we used a 2D PCA of the residual expression values. After batch correction, we found that dHSCs (146 SiCs from three plates) mixed across plates and also occurred in HSCs (173 SiCs from three plates; Figure S2C).

Single-cell RNA-seq data analysis

All analyses were performed based on the normalized and batch corrected expression data of the 4,707 variable genes.

Visualization and clustering

To visualize single cells and to explore the presence of possible sub-populations, we first generated a 2D heatmap using all 319 dHSCs and HSCs (using the R package gplots), and we applied PCA as well as a t-SNE to visualize the cells using 2D coordinates (van der Maaten and Hinton, 2008); using R package Rtsne). None of these approaches suggested that there is a discrete structure (Figures S2D–S2F). Since no distinct clusters were present in the tSNE and heatmap-based clustering analyses we used diffusion maps to visualize continuous transitions among the SiCs. Diffusion maps have been shown to organize individual cells according to their intrinsic stemness, while maintaining the global structure of cell-to-cell similarities. The diffusion map representation was generated using the R package destiny (Angerer et al., 2015).

In contrast to diffusion maps, PCA only captures linear effects. While this can result in reduced resolution of cell-cell similarities, PCA representations have a direct interpretation as linear projections. We visualized the genes driving variability along principal components one and two by plotting the five genes with largest positive and negative loadings for each PC, respectively.

Differential expression analysis and pathway enrichment

Genes that were differentially expressed between stages were identified using the Wilcoxon rank sum test, testing each stage versus all other stages. p values were corrected for multiple testing and considered statistically significant at a false discovery rate of 10%. Gene ontology (GO) enrichment was performed for up- and downregulated genes separately using the R package topGO and the elim algorithm (Bioconductor).

In addition to GO enrichment of differentially expressed genes, we also performed a pathway analysis based on the continuous expression values of cells assigned to individual stages. We used CAMERA (Wu and Smyth, 2012) to test whether a set of genes annotated to pathways form WikiPathways (Kutmon et al., 2016) is highly ranked relative to other genes in terms of differential expression. CAMERA heavily penalizes inter-gene correlation within groups based on the assumption it is not biologically relevant. However, this assumption does not hold for single-cell data where cells originate from a continuous biological process. As cells within the individual stages defined in our study are sampled from the continuous transition from dHSCs to active HSCs, even cells within stages can be ordered according to their intrinsic position on this trajectory. Consequently, we expect biologically relevant inter-gene correlations within each stage to remain and do not account for this inter-gene correlation.

To further explore additional gene signatures that have been reported to play a role in cell-cell-variability of HSCs, we assessed variability associated with a cell-cycle signature (Ashburner et al., 2000) and the recently described *MolO* signature (Wilson et al., 2015). We performed a PCA on the genes annotated to either gene signature, and visualized variation along the first principal component to identify differences in cell state related to each signature.

Pseudo-temporal analysis

We reconstructed the pseudo-temporal order of all HSCs and dHSCs by measuring transitions between cells using diffusion-like random walks (Haghverdi et al., 2016). We used the R package destiny to calculate diffusion pseudotime and visualized it in a diffusion map. We grouped cells into four stages in diffusion pseudo time by thresholding the inferred diffusion pseudo time at the 25%, 50% and 75% quantiles. To gain confidence that these stages were robust with respect to our normalization strategy, we repeated the same analysis using expression profiles that were size-factor normalized, resulting in robust stages (Figures 2B, S2B, and S2C).

We further assessed whether pathway activity changed significantly with pseudotime and performed a PCA on the genes annotated to a pathway from Wikipathways. Similar to the cell cycle analysis we used the first principal component to capture variation in cell states relative to individual pathways (pathway factors). We then tested for associations of the pathway activity with pseudotime. To this end, we modeled changes in pathway activity as a function of diffusion pseudotime by fitting a natural spline through the pathway factors using the Monocle package (Trapnell et al., 2014).

Cell cycle staging

We computationally assigned each cell to either G_0/G_1, S or G2/M phase. We applied the recently proposed Cyclone to calculate the probability for cells to be in each cell cycle phase, based on a random forest trained on cell cycle marker genes (https://github.com/PMBio/cyclone) (Scialdone et al., 2015).

Single-cell RNA-seq of HSC-Gpr^{pos}: mapping to SiC dHSCs/HSCs

52 single-cell HSCs-Gpr^{pos} from two independent experiments were sequenced, normalized and represented as described in *Single-cell RNA-seq Generation, Low Processing* and *Data Analysis*. Out of those 52 cells, 47 passed the quality control measures described in *Single-cell RNA-seq Low Level Processing.* Briefly, we generated a joint representation of HSCs, dHSCs and HSC-Gpr^{pos} by fitting a joint t-SNE and pseudotime representation comprising all cells.

Immunofluorescence staining of Cdk6

> 400 dHSC, aHSCs (defined as LSK CD150+ CD48- CD34- GFP^{pos}/^{neg} respectively) and MPP1 (defined as LSK CD150+ CD48- CD34+) from SCL-tTA;H2B-GFP mice chased with doxycycline for 150 days were FACS sorted as previously described (Wilson et al., 2008). dHSCs, aHSCs and MPP1s were seeded on fibronectin-coated glass coverslips and after a brief incubation in growth factor-free medium cells were fixed with BD Cytofix Fixation Buffer (BD Biosciences). After fixation cells were gently washed with PBS, permeabilized with 0.2% Triton X-100 (Sigma) in PBS for 20 min and blocked with 10% Donkey Serum (Sigma) for 30 min. Primary and secondary antibody incubations were performed for 1 hr at room temperature. Samples were imaged with an LSM710 confocal microscope (Zeiss) equipped with a 63X water objective. Primary raw data were imported into the Volocity Software package (Version 6.2, Perkin Elmer) for further processing and conversion into 3-dimensional images. The volume of the fluorescent signal was quantified across samples keeping threshold levels fixed. On average a total of 20 cells were singularly analyzed per sample. A total of 3 mice were used for these experiments. Primary antibodies used: anti-alpha tubulin (ab6160) from AbCam and anti-Cdk6 (ahz0232) from Invitrogen, Molecular Probes. Coverslips were mounted with ProLong Gold Antifade Reagent with DAPI (Invitrogen, Molecular Probes). The secondary antibodies were anti-rat DyLight488-conjugated antibody and anti-mouse Cy3-conjugated antibody (all obtained from Jackson ImmunoResearch).

Single-cell in vitro tracking of dHSC-aHSCs and HSCs-Gpr$^{pos/neg}$

600 HSCs (defined as LSK CD150+ CD48- CD34- GFP^{pos} /^{neg}) from SCL-tTA;H2B-GFP mice chased with doxycycline for 150 days were isolated by FACS as previously described (Wilson et al., 2008) in Complete Stem Cell Medium. Similarly, 600 HSCs (defined as LSK CD150+ CD48- CD34- EGFP^{pos} /^{neg}) from Gprc5c-EGFP mice were isolated by FACS in Stem Cell Medium. Of note, we used 6-8-month-old mice for both settings. HSCs were seeded in 24-well plates (StemSpan SFEM medium, StemCell Technologies, 100ng/ml SCF and TPO) equipped with silicon culture inserts (IBIDI). Plates were gas-tight sealed with adhesive tape after preincubation at 5% CO_2 / 37°C for at least 3 hr. Microscopy was performed using a CellObserver (Zeiss) at 37°C. Phase contrast images were acquired every 3 min using a 10x phase contrast objective (Zeiss), and an AxioCamHRm camera (at 1388x1040 pixel resolution) with a self-written VBA module remote controlling Zeiss AxioVision 4.8 software. Cell tracking was performed using a self-written computer program (TTT) as described elsewhere (Haetscher et al., 2015; Rieger et al., 2009; Thalheimer et al., 2014). The first mitosis of the purified HSCs was defined as time of first division. Dead cells were easily depicted by their shrunk, non-refracting appearance with immobility. All cell tracking was done by scientists; the current analysis does not rely on data generated by an unsupervised computer algorithm for automated tracking.

Gprc5c-EGFP experiments

Gprc5c-EGFP reversibility. Upon stress response

Gprc5c-EGFP mice were injected intraperitoneally with one dose of PBS or pIC (50 μg Poly(I:C)/mouse) as previously described (Essers et al., 2009). HSCs (defined as LSK CD150+ CD48- CD34- EGFP^{pos} /^{neg}) were analyzed 16 hr or 8 days after injection.

Gprc5c-EGFP reversibility upon serial stress response

Gprc5c-EGFP mice were injected intraperitoneally with two doses of PBS or pIC (50 μg Poly(I:C)/mouse) per week (days 0,2,7,9,14,16,19,21) for a total of three consecutive weeks (see workflow in Figure 3Q). Mice were kept 4 weeks to allow recovery. HSCs (defined as LSK CD150+ CD48- CD34- EGFP^{pos} /^{neg}) were analyzed 57 days after the first injection.

HSC-Gpr$^{pos/neg}$ Colony-Forming-Units (CFUs) assay

600 HSCs (defined as LSK CD150+ CD48- CD34- EGFP^{pos} /^{neg}) from 8-month old Gprc5c-EGFP mice were isolated using FACS and cultured in MethoCult M3434 (StemCell Technologies) in technical duplicates. 10 days after plating of CFUs, colony formation was quantified. 30,000 cells were used for replating and cultured in MethoCult M3434 (StemCell Technologies). 10 days after replating, colonies were quantified.

HSC-Gpr$^{pos/neg}$ transplant experiments

400 HSCs-Gpr^{pos} and Gpr^{neg} (defined as LSK CD150+ CD48- CD34- EGFP^{pos} /^{neg}) from 8-month old Gprc5c-EGFP (CD45.2) mice were FACS sorted and transplanted into irradiated (1 × 200 rad) NSG mice (CD45.1) together with $2x10^5$ supportive whole BM cells (CD45.1/2). Contribution of CD45.2-donor cells was monitored in peripheral blood at 4, 8 and 16 weeks post-transplantation in primary and secondary recipients (Figure 3N). Outcome was addressed by flow cytometry using the following monoclonal antibodies: anti-CD45.1 (A20)–PECy7; anti-CD45.2 (104)–PB. For secondary transplantations, whole BM was isolated at 16 weeks

post-transplantation and 3x10^6 cells were re-transplanted into irradiated (1 × 200 rad) NSG (CD45.1) recipient mice. *Multipotency*. 16-weeks after the 1st transplant, peripheral blood of transplanted animals was stained with the following monoclonal antibodies: anti-CD45.1 (A20)–PECy7, anti-CD45.2 (104)–PB, anti-CD11b (M1/70)-AF700, anti-GR1 (RB6.8C5)-APC-Cy7, anti-CD8a (53.6.7)-PE, anti-CD4 (GK1.5)-PE, anti-B220 (RA3.6B2)-PE-Cy5. Total myeloid, B- and T cells numbers were normalized to 100% as described (Cabezas-Wallscheid et al., 2014).

Cell cycle analysis

HSC surface staining defined as (LSK CD150+ CD48- CD34- EGFP^{pos} /^{neg}) was performed on Gprc5c-EGFP bone marrow cells. Cells were fixed with BD Cytofix/Cytoperm Buffer (Beckton Dickinson). Subsequently, intracellular Ki-67 (BD Biosciences) staining was performed using PermWash solution (Beckton Dickinson). Prior to flow cytometry analysis cells were stained with Hoechst 33342 (Invitrogen).

ATRA in vitro experiments

Enrichment HSPCs

To enrich HSPCs for in vitro assays, lineage marker (CD4, CD8a, B220, Gr-1, CD11b, Ter119)-positive and CD48-positive cells were depleted from bone marrow using biotin-labeled antibodies and biotin binder streptavidin Dynabeads (Invitrogen). For bone marrow preparation, see above.

HSPCs plating and treatment

HSPCs from SCL-tTA;H2B-GFP, Gprc5c-EGFP, Myc-GFP and Mito-roGFP2-Orp1 mice were cultured in Complete Stem Cell Medium (StemPro-34 SFM, LifeTechnologies containing 50 ng/ml SCF, 25 ng/ml TPO, 30 ng/ml Flt3-Ligand (all Preprotech), 100 u/ml Penicillin/Streptomycin, 2 mM L-Glutamine). Cells were cultured in 6-well ultralow attachment plates and were treated with either ATRA (Sigma-Aldrich) (5 μM), Retinol (Sigma-Aldrich) (10 μM) or Myc inhibitor (Calbiochem) (53.3 μM) or the respective amount of DMSO.

Colony-Forming-Unit assays (CFUs) of ATRA treated cells

1,000 FACS-sorted LSK cells from 8-12-week-old mice or 400 FACS-sorted HSC-Gpr$^{pos/neg}$ cells were FACS sorted and cultured in 100 μl Complete Stem Cell Medium (described in *HSPCs Plating and Treatment*) in 96 well ultra-low attachment plates and immediately treated with ATRA (5 μM) or the respective amount of DMSO. 72h after treatment, all cells of one well were harvested and cultured in MethoCult M3434 (StemCell Technologies). 9 Days after plating of CFUs, colony formation was quantified. 30,000 cells of each replicate were used for replating and cultured in MethoCult M3434 (StemCell Technologies). 5 days after replating, colonies were quantified.

Serial transplantation experiments of ATRA treated cells

1,000 LSK cells from 8-12-week-old mice were FACS sorted and cultured in 100 μl Complete Stem Cell Medium (described in *HSPCs Plating and Treatment*) in 96 well ultra-low attachment plates and immediately treated with ATRA (5 μM) or the respective amount of DMSO. 72h after treatment, all cells of one well were harvested and transplanted into fully irradiated (2 × 4.5 Gy.) B6 mice (CD45.1) together with 1x10^5 supportive whole BM cells (CD45.1/2). Contribution of CD45.2-donor cells was monitored in peripheral blood at 4, 8, 12 and 16 weeks' post-transplantation in primary and secondary recipients (Figure 4L). Outcome was addressed by flow cytometry using the following monoclonal antibodies: anti-CD45.1 (A20)–PECy7; anti-CD45.2 (104)–PB. For secondary transplantations, whole BM was isolated 16 weeks post-transplantation and 3x10^6 cells were re-transplanted into fully irradiated (2 × 4.5 Gy.) B6 mice (CD45.1).

HSCs-Gpr$^{pos/neg}$ and treatment

500 FACS-sorted *HSCs-Gpr$^{pos/neg}$* from 6-month old Gprc5c-EGFP mice were cultured in Complete Stem Cell Medium (StemPro-34 SFM, LifeTechnologies containing 50 ng/ml SCF, 25 ng/ml TPO, 30 ng/ml Flt3-Ligand (all Preprotech), 100 u/ml Penicillin/Streptomycin, 2 mM L-Glutamine). Cells were cultured in 96-well ultralow attachment plates and were treated with either ATRA (Sigma-Aldrich) (10 μM), Retinol (10 μM) or the respective amount of DMSO for 24h.

Caspase-3 staining

For active Caspase 3 staining, cells were fixed and permeabilized using Cytofix/Cytoperm (Beckton Dickinson) after surface staining (LSK CD150+ CD48- CD34-). Intracellular staining with the anti-active Caspase 3-PE antibody (BD PharMingen) was performed over night at 4°C in PermWash solution (Beckton Dickinson).

OP-Puro measurement

Analysis of OP-Puro Incorporation using the Click-iT Technology. To measure protein synthesis, in vitro ATRA/DMSO-cultured HSPCs (described in *HSPCs Plating and Treatment*) were incubated for 1h in medium supplemented with O-propargyl-puromycin (OP-Puro) (Jena Biosciences, 50 μM final concentration). After harvesting, cells were surface-stained to enable specific analysis of LSK CD48- CD34- cells. Subsequently, the cells were fixed for 15 min at 4°C in PBS supplemented with 4% paraformaldehyde (Electron Microscopy Sciences, 19208) and then permeabilized in PBS supplemented with 1% bovine serum albumin (BSA) and 0.1% saponin by performing two washing steps. The copper-catalyzed azide-alkyne cycloaddition (CuAAC) was performed using an Alexa647-azide (Life Technologies, 5 μM final concentration) and the Click-iT Cell Reaction Buffer Kit (Life Technologies) according to the manufacturer's instructions.

ROS measurement

The Mito-roGFP2-Orp1 probe allows the qualitative measurement of H_2O_2 levels in mitochondrial matrix of intact living cells (Fujikawa et al., 2016). Fluorescence ratios (405/488 nm) were measured using a fluorescence microplate reader (PHERAstar FS, BMG Labtech) employing 10^5 enriched HSPCs expressing mito-roGFP2-Orp1 either freshly isolated (0h), in vitro DMSO-cultured (24h, Control) or ATRA-cultured cells (24h, ATRA; described in *HSPCs Plating and Treatment*). As control, samples were treated with 2mM diamide (Sigma-Aldrich) (fully oxidized) and 10 mM DTT (Applichem) (fully reduced). 405/488 nm raw ratio values were converted to OxD values as previously described (Meyer and Dick, 2010).

Gene expression of in vitro ATRA treated HSCs by microarray analysis

A total of 4-5 mice were pooled for each replicate. Total of 3 replicates per condition, in 3 independent sorts. Enriched HSPCs from C57BL/6 J wild-type mice were cultured in Complete Stem Cell Medium as described above. 24 hr later, 10,000 HSCs were FACS sorted into RNA lysis buffer. HSC surface staining defined as LSK $CD150^+CD48^-CD34^-$. Total RNA was isolated as described above. All samples showed a RIN value > 9 (data not shown). Samples were normalized to RNA amount. We discarded one sample (HSC ATRA-treated) based on the poor quality of the sample. *Microarray Chip*. Microarray gene-expression analysis was made using the GeneChip Mouse Gene 2.0 ST Array (Affymetrix). Raw images and CEL intensity files were generated with the Affymetrix Gene Chip Operating Software (GCOS). Quality control, RMA background subtraction, quantile normalization and summarization of the intensity data have been made with the Bioconductor oligo package under the statistical software R (http://www.r-project.org). Differentially expressed genes (DEG) have been calculated using the Limma package. *GSEA analysis*. For statistical quantification, permutation testing in GSEA was performed with 1,000 permutations by gene set.

Gene expression analysis by qPCR

For Real-time PCR, total RNA was isolated as described above and reverse-transcribed using SuperScript VILO cDNA Synthesis Kit (Invitrogen) according to manufacturer's guidelines. For qRT-PCR analysis, Fast SYBR Green Master Mix was used on a ViiA 7 Real-Time PCR System (Applied Biosystems). RNA expression was normalized to Oaz1 housekeeping gene expression and presented as relative quantification (Ratio = $2^{-\Delta\Delta CT}$). Primers were designed using the Universal ProbeLibrary Assay Design Center (Roche). For list of primers see Table S5. The analysis of amplification curves was carried out using the ViAA 7 Software v1.1 (Applied Biosystems).

ATRA in vivo experiments

In vivo treatment

Gprc5c-EGFP, Mito-roGFP2-Orp1 and C57BL/6J wild-type mice were intraperitoneally injected with 30 mg/kg of either ATRA or the respective amount of DMSO in 200 μl PBS. 7h later mice were injected intraperitoneally with 50 μg Poly(I:C), 5 μg LPS from *Escherichia coli* (Sigma-Aldrich) or PBS alone. 16h later, mice were sacrificed and further analyzed. For 5-FU treatment, C57BL/6 J wild-type mice were intraperitoneally injected with 150 mg/kg 5-FU (Sigma-Aldrich). 24h and 48h later mice were intraperitoneally injected with 30 mg/kg of either ATRA or the respective amount of DMSO in 200 μl PBS. Mice were analyzed 72h later. This protocol was adapted based on timing of HSC activation upon 5-FU treatment (Venezia et al., 2004).

ROS measurement

As described before (in vitro *ROS measurement)*, fluorescence ratios (405/488 nm) were measured using a fluorescence microplate reader (PHERAstar FS, BMG Labtech) employing 10^5 enriched HSPCs expressing mito-roGFP2-Orp1 of ATRA and control treated cells upon in vivo pIC treatment (described in in vivo *treatment*). As control, samples were treated with 2 mM Diamide (Sigma-Aldrich) (fully oxidized) and 10 mM DTT (Applichem) (fully reduced). 405/488 nm raw ratio values were converted to OxD values as previously described (Meyer and Dick, 2010).

Gene expression of in vivo ATRA ± pIC treated HSCs by microarray analysis

C57BL/6 J wild-type mice were intraperitoneally injected with 30 mg/kg of either ATRA or the respective amount of DMSO in 200 μl PBS. 7h later mice were injected intraperitoneally with 50 μg Poly(I:C) or PBS alone. 16h later, mice were sacrificed and > 2,500 HSCs were FACS-sorted into RNA lysis buffer. HSC surface staining defined as (LSK CD150+ CD48- CD34-). A total of 2 mice were pooled for each replicate. Total of 2-3 replicates per condition. Total RNA was isolated as described above. All samples showed a RIN value > 9 (data not shown). Samples were normalized to RNA amount. *Microarray Chip*. Microarray gene-expression analysis was done using the GeneChip Mouse Gene 2.0 ST Array (Affymetrix, Santa Clara, CA, USA). Raw images and CEL intensity files were generated with the Affymetrix Gene Chip Operating Software (GCOS). Quality control, RMA background subtraction, quantile normalization, and summarization of the intensity data have been made with the Bioconductor oligo package under the statistical software R (http://www.r-project.org). Differentially expressed genes (DEG) were calculated using the Limma package. Genes with a FDR < 0.1 were selected for further analysis. Gene Ontology (GO) analysis was performed via hypergeometric tests under the GOstats package. Heatmaps were generated with the heatmap.2 function of the gplots package. *GSEA analysis*. For statistical quantification, permutation testing in GSEA was performed with 1,000 permutations by gene set.

Colony-Forming-Unit assays (CFU)s of in vivo ATRA treated cells

C57BL/6 J wild-type mice were intraperitoneally injected with 30 mg/kg of either ATRA or the respective amount of DMSO in 200 μl PBS. 7h later mice were injected intraperitoneally with 50 μg Poly(I:C) or PBS alone. 16h later, mice were sacrificed and $4x10^4$ whole bone marrow cells from in vivo Control, ATRA, Control+pIC, ATRA+pIC treated mice were cultured in MethoCult M3434 (StemCell Technologies). 7 Days after plating of CFUs, colony formation was quantified.

Vitamin A free diet

Vitamin A free diet in homeostatic settings

3-4-week old mice were put in a vitamin A free diet (Altromin International GmbH & Co) for 14 to 17 weeks (N = 12). Littermate controls were fed with regular food and analyzed the same day (N = 9). 2 independent experiments.

Peripheral blood analysis

Peripheral blood counts were analyzed using the HEMAVET 1700 device according to manufacturer's instructions (Drew Scientific Group).

Analysis of bone marrow differentiated cells

$5x10^6$ bone marrow cells from mice kept in vitamin A free diet and regular diet were stained with the following monoclonal antibodies: anti-CD11b (M1/70)-APC-Cy7, anti-GR1 (RB6.8C5)-APC, anti-CD8a (53.6.7)-PB, anti-CD4(GK1.5)-PB, anti-B220 (RA3.6B2)-AF700, IgM(II-41)-PECy5, CD71(R17217)-PE. Total myeloid, B- and T cells outcome was normalized to 100% as described (Cabezas-Wallscheid et al., 2014).

Serial Colony-Forming-Unit assays (CFU)s of Vitamin A free diet BM cells

$4x10^4$ whole bone marrow cells from mice kept in vitamin A free diet and regular diet were cultured in MethoCult M3434 (StemCell Technologies). 7 Days after plating of CFUs, colony formation was quantified. In each plating: 30,000 cells of each replicate were used for 2^{nd}, 3^{rd} and 4^{th} plating and cultured in MethoCult M3434 (StemCell Technologies). 7, 5 and 5 days after replating respectively, colonies were quantified.

Transplantation experiments of vitamin A free diet cells

$2x10^5$ whole bone marrow cells from C57BL/6 J wild-type mice kept on a vitamin A free diet for 14 weeks or on a regular diet were transplanted into fully irradiated (2 × 4.5 Gy.) CD45.1/2 mice in competition to $2x10^5$ whole bone marrow cells from 4-5-month old CD45.1 mice (same age as competitor) within 24h after irradiation by tail vein injection. As quality control, contribution of CD45.2 versus CD45.1 was analyzed prior to transplantation by FACS. Contribution of CD45.2-donor cells was monitored in peripheral blood at 4, 8, 12 and 16 weeks post-transplantation. Outcome was addressed by flow cytometry using the following monoclonal antibodies: anti-CD45.1 (A20)–PECy7, anti-CD45.2 (104)–PB, anti-CD11b (M1/70)-AF700, anti-GR1 (RB6.8C5)-APC-Cy7, anti-CD8a (53.6.7)-PE, anti-CD4 (GK1.5)-PE, anti-B220 (RA3.6B2)-PE-Cy5. Radioresistant cells (CD45.1/2) were gated out to avoid potential irradiation inconsistencies.

Gene expression of vitamin A free diet HSCs and MPPs by qPCR analysis

Mice kept on a vitamin A free diet for 14 weeks or regular diet were sacrificed and > 3,500 HSCs and MPP3/4 were FACS sorted into RNA extraction buffer. HSC surface staining defined as LSK $CD150^+CD48^-CD34^-$, and MPP3/4 as LSK $CD150^+CD48^+$. A total of 2 mice were pooled for each replicate. Total of 3 replicates per condition. Total RNA was isolated and qPCR was performed as described above.

Vitamin A free diet in reversibility experiments

3 to 4-week old mice were put on a vitamin A free diet for 14 weeks (N = 10). Littermate controls were fed with regular food and analyzed the same day (N = 8). 8-11 days before endpoint analysis mice were injected intraperitoneally with 50 μg Poly(I:C) or PBS alone. Of note, in each group 20% of mice were kept in vitamin A free diet or regular diet as control. 2 independent experiments.

QUANTIFICATION AND STATISTICAL ANALYSIS

Statistical analysis was performed by unpaired Student's t test or two- or one-way ANOVA without correction for multiple comparison (Fisher LSD test). All data are presented as mean ± SEM. Significance levels were set at $p^* < 0.05$, $p^{**} < 0.01$ and $p^{***} < 0.001$. For statistical analysis GraphPad Prism was used.

DATA AND SOFTWARE AVAILABILITY

The accession number for the population RNA-seq data of dHSCs, aHSCs, and MPP1 reported in this paper is ArrayExpress: E-MTAB-4549. The accession number for the single-cell RNA-seq data of dHSCs and HSCs reported in this paper is ArrayExpress: E-MTAB-4547. The accession number for the microarray data of in vitro and in vivo treatment with ATRA reported in this paper is GEO: GSE87814. A detailed description of data analyses and software used for each section can be found in METHODS DETAILS.

Cell

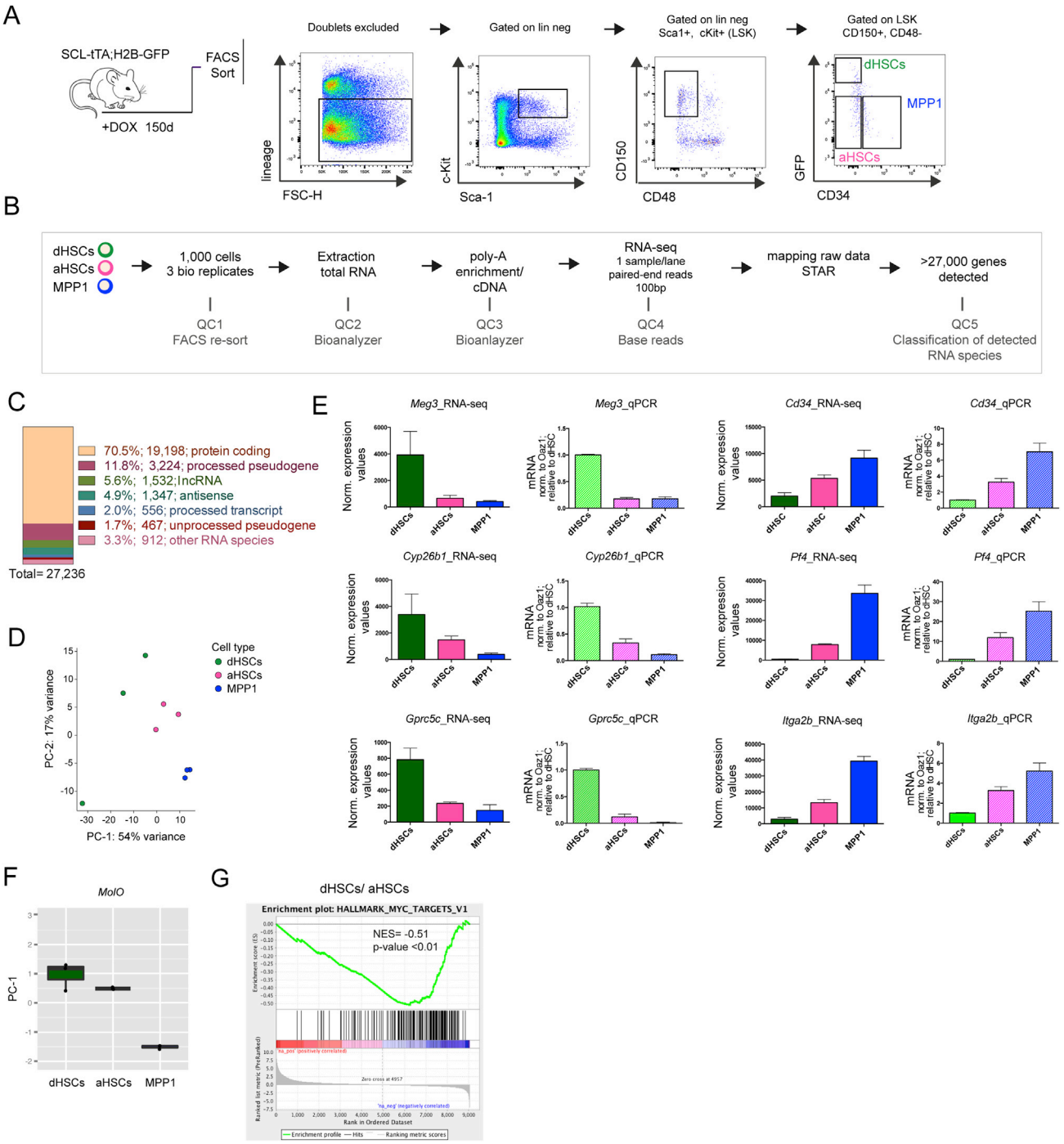

Figure S1. Population RNA-Seq of dHSCs, aHSCs, and MPP1, Related to Figure 1

(A) Workflow for FACS sorting dHSCs, aHSCs and MPP1 cells. Mouse model and gating strategy for FACS cell sorting are shown.

(B) RNA-seq workflow. Quality controls (QC) for RNA-seq. QC1-QC5 were carried out as indicated and as previously described (Cabezas-Wallscheid et al., 2014; Klimmeck et al., 2014).

(C) RNA categories of 27,236 quantified genes. Percentage and number of RNA species within each RNA class. Of note, gene quantified = mean counts > 0 in at least one sample.

(D) Principal component analysis. The first two principal axes are shown.

(E) Validation of RNA-seq results for differentially expressed genes by qPCR. Average ± SEM is shown. N = 3.

(F) Principal component analysis (PCA). Molecularly overlapping population (*MolO*) signature based on (Wilson et al., 2015). One component is represented.

(G) Gene set enrichment analysis (GSEA). NES = Normalized Enrichment Score. dHSCs versus aHSCs is represented. Further details in STAR Methods.

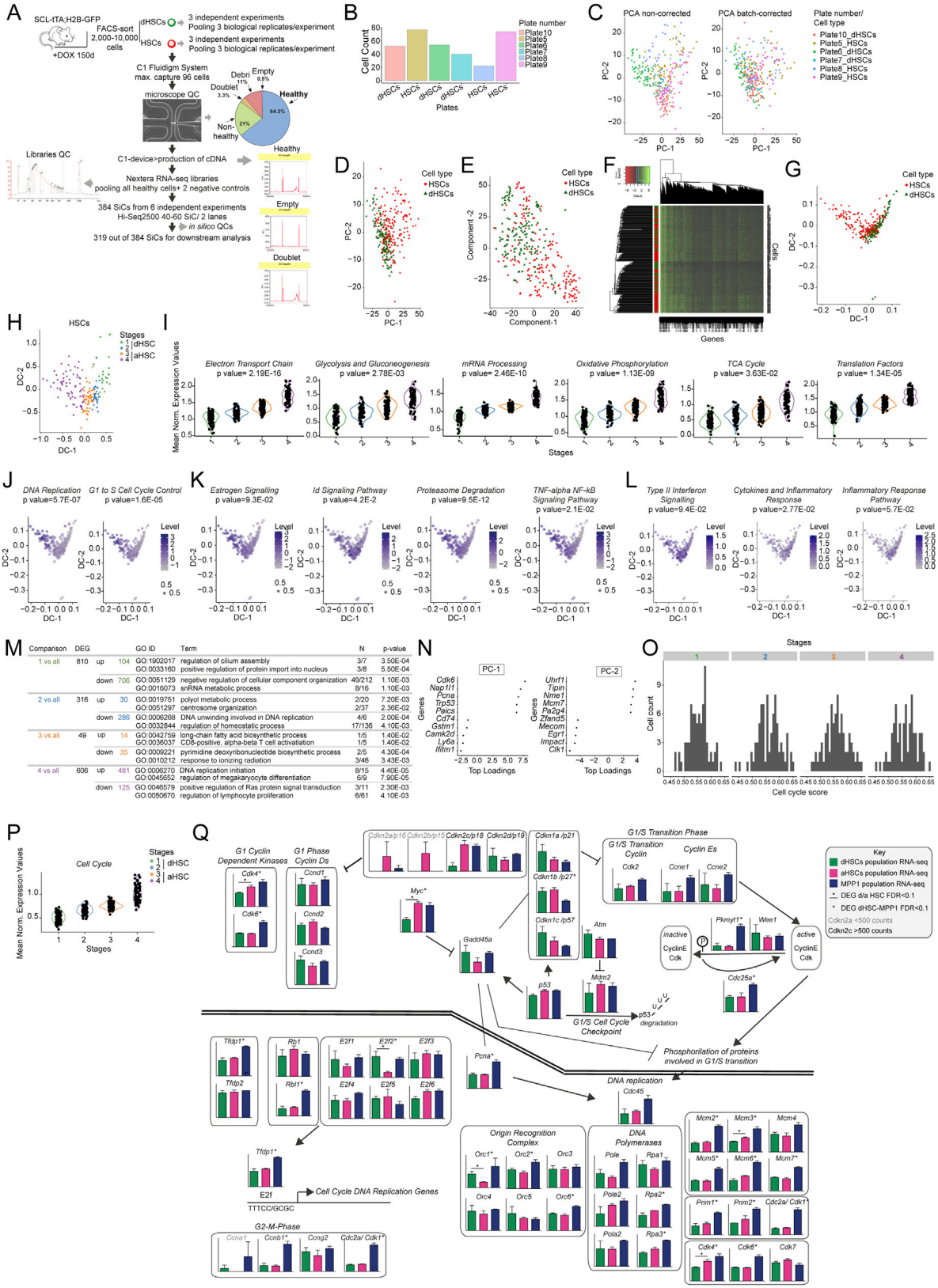

(legend on next page)

Figure S2. Single-Cell RNA-Seq of dHSCs and Overall HSCs, Related to Figure 2

(A) Single-cell RNA-seq workflow. Mouse model, steps to generate single-cell (SiC) raw data and quality controls (QC) are indicated. Representative Bioanalyzer results are depicted. Either dHSC (Lineage$^-$ Sca-1$^+$ c-Kit$^+$ (LSK), CD150$^+$, CD48$^-$, CD34$^-$, GFP^{pos}) and HSCs (LSK, CD150$^+$, CD48$^-$, CD34$^-$) were sorted from SCL-tTA;H2B-GFP mice after 150 days chasing (further details in STAR Methods).

(B) Cell count per sequenced plate. Plate numbers refer to the experiment number and are arbitrary numbers.

(C) Principle component analysis (PCA) non-corrected and batch corrected. Each dot represents one cell. Cells across 6 sequenced plates are represented before and after batch correction. Plate numbers refer to the experiment number and are arbitrary numbers.

(D) Principle component analysis (PCA) of dHSC and HSCs. Each dot represents one cell. Sorted HSCs (circles) and dHSCs (triangles). Of note, no distinct clusters are observed.

(E) TSNE-based visualization. Each dot represents one cell. Sorted HSCs (circles) and dHSCs (triangles). Of note, no distinct clusters are observed.

(F) Heatmap. All sequenced cells and detected genes are depicted. Of note, no distinct clusters are observed supporting continuum-like pattern in the transition from dormant toward active HSCs.

(G) Diffusion map representation. Each dot represents one cell. Sorted HSCs (circles) and dHSCs (triangles). Coloring indicates dHSCs and HSCs. A continuum-like pattern from dormant toward active HSCs is observed.

(H) Diffusion map representation of only HSCs. Representation of HSCs (no representation of sorted dHSCs). Each dot represents one cell. Coloring is derived from partitioning DPT of all cells into four stages: 1 to 2 mostly enriched in dHSCs; 3 to 4 mostly enriched in aHSCs. DC-1, 2, diffusion component 1, 2. Of note, a continuum-like pattern from dormant (1) toward active (4) HSCs is observed mimicking the in vivo situation.

(I) Signaling pathway enrichment analysis within stage 1 to 4 represented with violin plots. From dormant to active HSCs (FDR < 0.1; arbitrary units: mean normalized expression values). Each dot represents one cell.

(J–L) Diffusion map representation of differential pathways. Of note, (J) cell cycle and (K) other processes follow a gradual transition from most dormant toward active HSCs. (L) Pathways which do not follow a gradual transition. Each dot represents one cell. Colors encode standardized pathway activity. FDR < 0.1.

(M) Overrepresented biological processes in each stage. Differentially expressed genes (DEG) from each stage against the rest. Top two up and down enriched processes are represented.

(N) Top loadings for each component. Most relevant genes driving principle component 1 and 2 are represented. See also (D). Norm., normalized.

(O) Cell cycle score distribution of each stage. From dormant stage 1 to active stage 4.

(P) Principal component analysis. Cell cycle signature represented with violin plots. One component is represented. Mean normalized expression values.

(Q) Cell cycle processes. Normalized RNA expression values ± SEM are shown (arbitrary units); DEG = differentially expressed genes. Of note, analysis based on dHSC, aHSC and MPP1 bulk RNA-seq data (Table S1) since population RNA-seq data also includes the multipotent progenitor MPP1 data. Further details in STAR Methods.

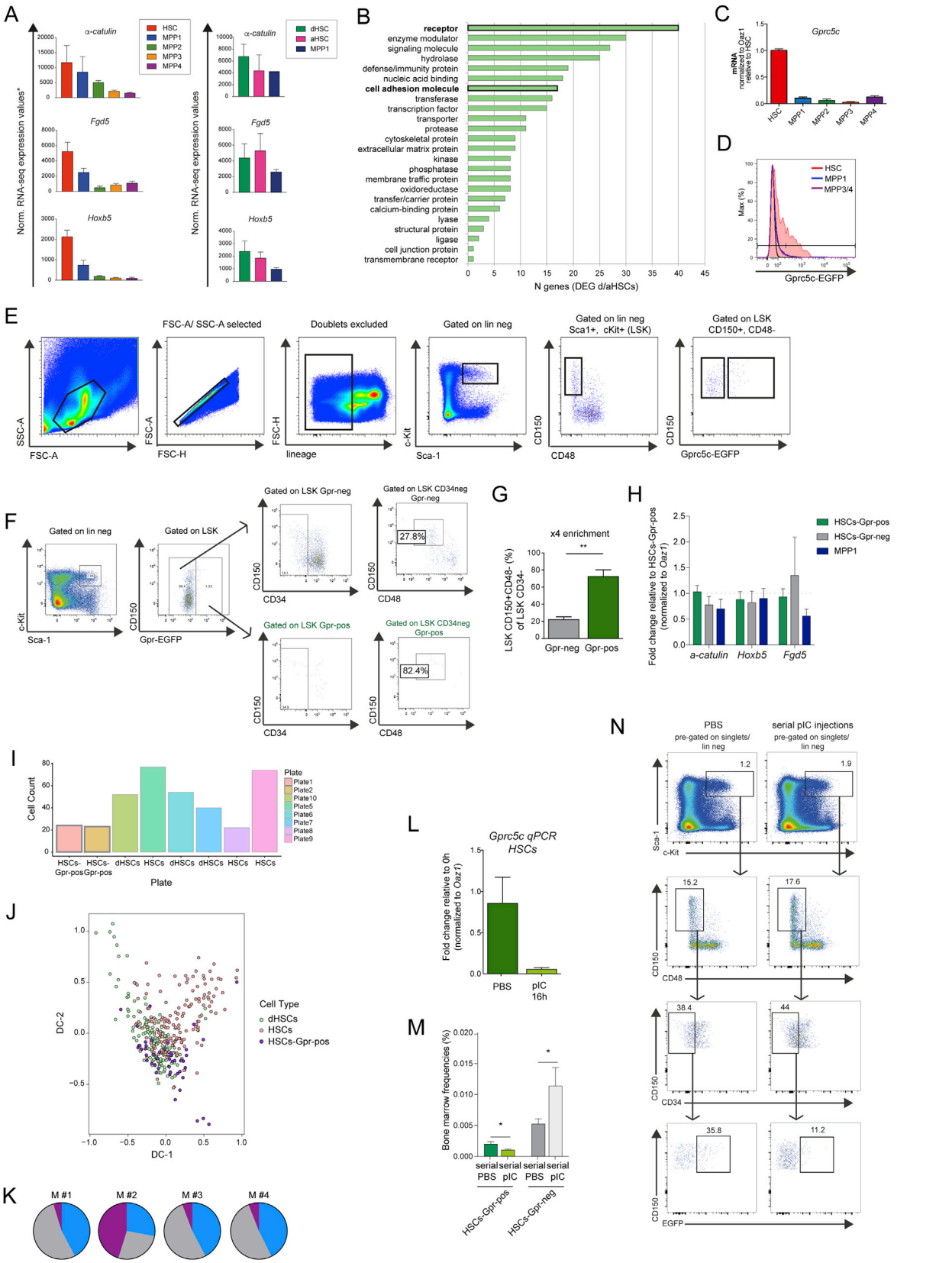

(legend on next page)

Figure S3. Characterization of the Gprc5c-EGFP Reporter Mouse Model, Related to Figure 3

(A) Gene expression patterns of published HSC-reporter mouse models in HSC-MPPs and dHSC, aHSC and MPP1. RNA-seq normalized mean expression in HSCs, MPP1, MPP2, MPP3, MPP4 of published HSC-reporter mouse models (*α-catulin*, *Hoxb5* and *Fgd5*; (Acar et al., 2015; Chen et al., 2016; Gazit et al., 2014a) respectively) based on Cabezas-Wallscheid et al. (2014). Similarly, expression of HSC-reporter mouse models in dHSC, aHSC and MPP1 RNA-seq data.

(B) Classification of dHSC enriched genes according to protein class. 236 significantly higher expressed genes in dHSCs compared to aHSCs (FDR < 0.1) were subjected to protein classification according to the Gene Ontology tool Panther.

(C) Validation of RNA-seq results for Gprc5c by qPCR (HSC-MPPs, nomenclature and sorting scheme as previously described (Lipka et al., 2014). N = 3-4.

(D) Representative FACS histogram plot for Gprc5c-EGFP expression. Pre-gated on HSC (LSK $CD150^{+}CD48^{-}CD34^{-}$), MPP1 (LSK $CD150^{+}CD48^{-}CD34^{+}$), MPP3/4 (LSK $CD150^{-}CD48^{+}CD34^{+}$).

(E) Representative FACS dot plots of HSC-$Gpr^{pos/neg}$.

(F) Representative FACS dot plots of Gpr enrichment based on other stem cell markers.

(G) Percent of LSK $CD150^{+}CD48^{-}$ based on LKS $CD34^{-}$ pre-gating and $Gpr^{pos/neg}$. N = 3.

(H) Gene expression patterns in HSCs-Gpr^{pos}, HSCs-Gpr^{neg} and MPP1 of published HSC-reporter mouse models. QPCR data. N = 5-6.

(I) Cell count per sequenced plate. C1-plate numbers refer to the experiment number. Of note, for HSCs-Gpr^{pos} two independent experiments were performed.

(J) Diffusion map including HSC-Gpr^{pos}, dHSCs and HSCs. Of note, HSC-Gpr^{pos} localize within dHSCs in line with Figure 3I.

(K) Multipotency. Relative outcome of myeloid and lymphoid (B- and T cells) in peripheral blood of individual HSC-Gpr-pos mice 16 weeks after 1^{st} transplant.

(L) Validation of HSC-Gpr^{pos} cells before and after pIC injection by qPCR. N = 3.

(M) HSC frequencies upon serial pIC treatment. N = 4.

(N) Representative FACS dot plots of PBS and serial pIC activated mice. Numbers represent relative percent within each gate. For all panels, average ± SEM is shown. *, **$p < 0.05$ and 0.01 respectively. n.s. non significant. N indicates biological replicates. Further details in STAR Methods.

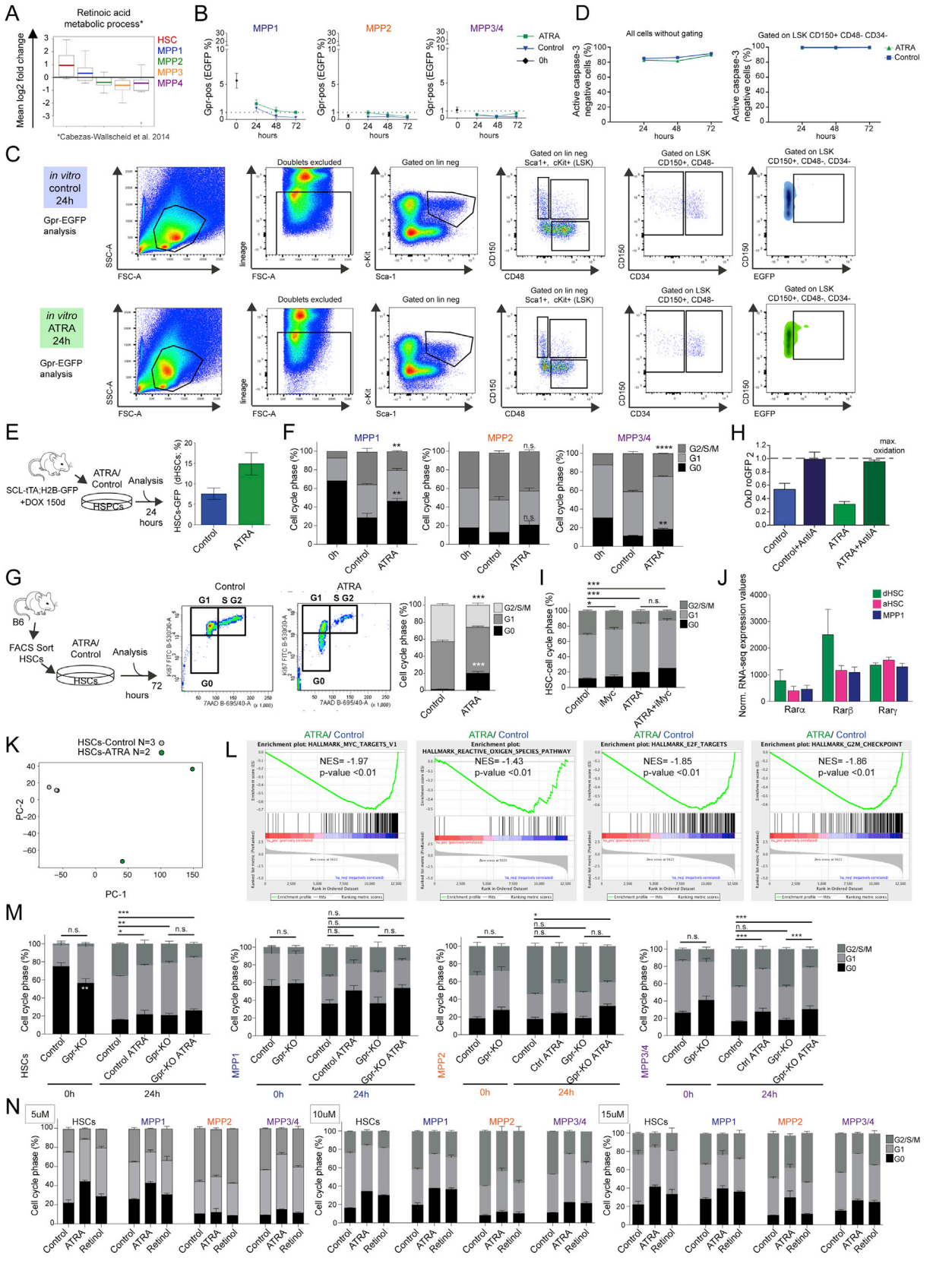

(legend on next page)

Figure S4. Retinoic Acid Treatment In Vitro, Related to Figure 4

(A) Retinoic acid metabolism in HSC to MPP4. HSC to MPP4 RNA-seq normalized mean expression of retinoic acid (RA) metabolism based on Cabezas-Wallscheid et al., 2014.

(B) *Gprc5c* expression upon in vitro ATRA treatment. Percentage of EGFP within MPP1, MPP2, MPP3/4 is represented. N = 4-5. Gated on MPP1 (LSK $CD150^{+}CD48^{-}CD34^{+}EGFP^{+}$), MPP2 (LSK $CD150^{+}CD48^{+}EGFP^{+}$), MPP3/4 (LSK $CD150^{-}CD48^{+}EGFP^{+}$).

(C) Representative FACS dot plots of in vitro ATRA-treated and non-treated cells.

(D) Cell viability measured by FACS based on active caspase-3 staining. Left panel, all cells without gating. Right panel, pre-gated on HSCs (LSK CD150+ CD48-CD34-). Of note, no differences between ATRA treated and non-treated cells were observed. N = 3.

(E) dHSC/LR cells upon in vitro ATRA treatment. Left panel, workflow. Right panel, results. Percentage of GFP within HSCs is represented. N = 2.

(F) Cell cycle analysis upon in vitro ATRA treatment. Gated on MPP1 (LSK $CD150^{+}CD48^{-}CD34^{+}$), MPP2 (LSK $CD150^{+}CD48^{+}$), MPP3/4 (LSK $CD150^{-}CD48^{+}$). Right panel, relative percentage within each cell cycle phase. N = 3-6.

(G) in vitro ATRA treatment of FACS-sorted HSCs. Left panel, workflow. Middle panel, representative FACS dot plots. Right panel, cell cycle analysis. Relative percentage within each cell cycle phase is shown. N = 4.

(H) Degree of oxidation (OxD) upon stimulation with antimycin A in control and ATRA treated cells. Of note, blocking the respiratory chain complex III with antimycin A lead to complete mitochondrial probe oxidation independently of ATRA treatment, thus confirming that mito-roGFP2-Orp1 maintains responsiveness to endogenous H_2O_2 under both conditions. N = 2.

(I) Cell cycle profile upon simultaneous in vitro Myc-inhibitor and ATRA treatment. Relative percentage within each cell cycle phase within HSCs is represented. N = 2.

(J) RNA-seq expression of retinoic acid receptors (Rar) in dHSC, aHSC and MPP1. Normalized RNA-seq expression (arbitrary units). N = 3.

(K) Principal component analysis. The first two principal axes are shown.

(L) Gene set enrichment analysis (GSEA). NES = Normalized Enrichment Score. ATRA-treated versus untreated HSCs is represented. Further details on GSEA analysis in STAR Methods.

(M) Cell cycle analysis of Gprc5c-KO HSPCs upon ATRA treatment. Relative percentage within each cell cycle phase. N = 3. Gpr-KO = Gprc5c knockout cells.

(N) Retinol Titration. Cell cycle analysis using 5, 10 and 15 μM of retinol. Relative percentage within each cell cycle phase. N = 2. Of note, 5 μM has no effect. We used 10 μM for further experiments. For all panels, +/− SEM is shown. *, **, ***, ****$p < 0.05$, 0.01, 0.001 and 0.0001 respectively. n.s. non-significant. N indicates biological replicates. Further details in STAR Methods.

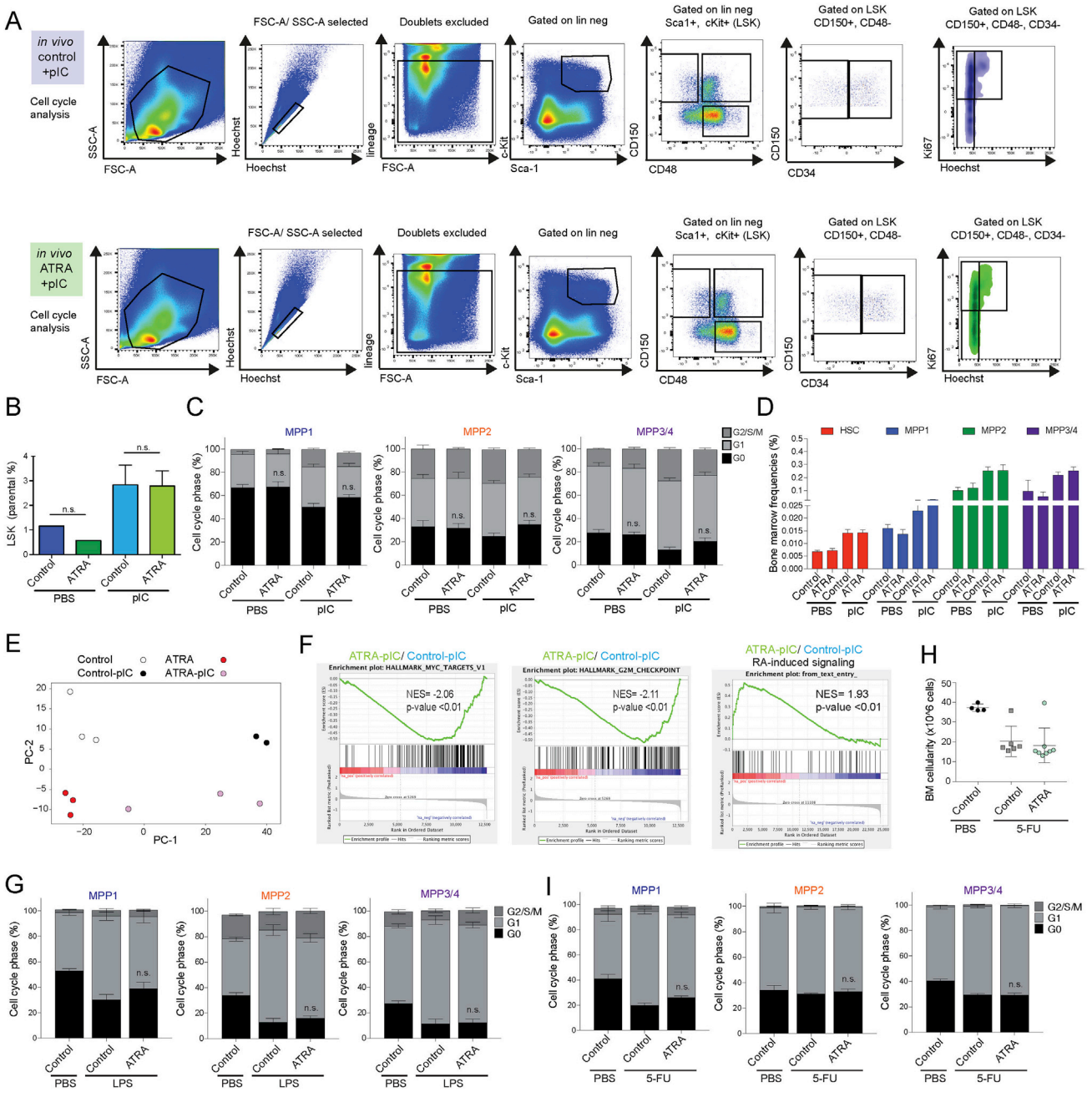

Figure S5. Retinoic Acid Treatment In Vivo, Related to Figure 5

(A) Representative FACS dot plots of in vivo ATRA-treated and non-treated mice after one pIC injection. Of note, control samples show higher percentage of cycling cells.

(B) Percentage of LSK cells in controls (PBS injected) and upon stress (pIC injected). N = 5.

(C) Cell cycle analysis upon in vivo ATRA treatment in homeostasis and pIC-induced stress. Gated on MPP1 (LSK $CD150^{+}CD48^{-}CD34^{+}$), MPP2 (LSK $CD150^{+}CD48^{+}$), MPP3/4 (LSK $CD150^{-}CD48^{+}$).

(D) HSC, MPP1, MPP2, MPP3/4 frequencies. Percentage of bone marrow HSC-MPPs are represented. N = 4-8.

(E) Principal component analysis. The first two principal components are shown.

(F) Gene set enrichment analysis (GSEA). NES = Normalized Enrichment Score. ATRA/pIC-treated versus pIC-treated HSCs is represented. Further details on GSEA analysis in STAR Methods.

(G) Cell cycle analysis upon in vivo ATRA treatment in homeostasis and LPS-induced stress. Gated on MPP1 (LSK $CD150^{+}CD48^{-}CD34^{+}$), MPP2 (LSK $CD150^{+}CD48^{+}$), MPP3/4 (LSK $CD150^{-}CD48^{+}$).

(H) BM cellularity in control and upon 5-FU treatment.

(legend continued on next page)

(l) Cell cycle analysis upon in vivo ATRA treatment in homeostasis and 5-FU-induced stress. Gated on MPP1 (LSK $CD150^{+}CD48^{-}CD34^{+}$), MPP2 (LSK $CD150^{+}CD48^{+}$), MPP3/4 (LSK $CD150^{-}CD48^{+}$).

For all panels, +/− SEM is shown. n.s. non-significant. For all experiments, greater than or equal to 2 independent experiments were performed otherwise indicated. Further details in STAR Methods.

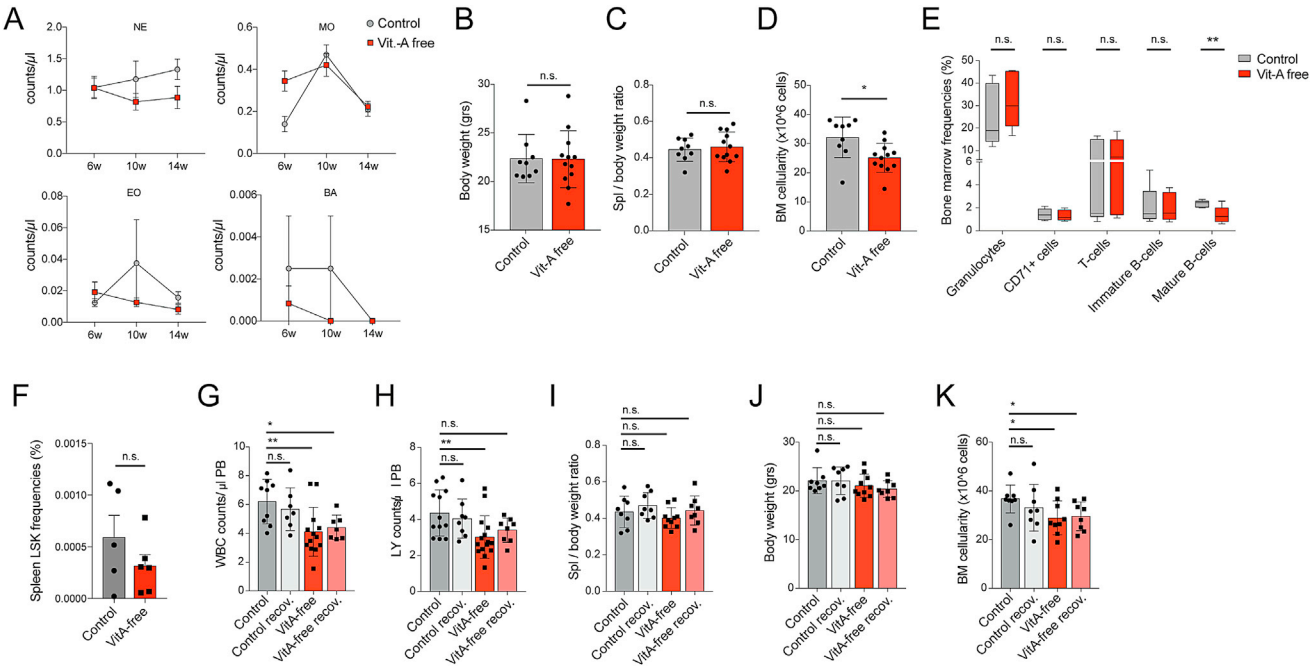

Figure S6. Vitamin A-Deficient Diet, Related to Figure 6

(A) Peripheral blood analysis overtime. N = 6. NE = neutrophils. MO = monocytes; EO = eosinophils. BA = basophils. 6 to 17 weeks (w).

(B) Body weight.

(C) Spl/body ratio. Spl = spleen.

(D) BM cellularity.

(E) Frequencies of differentiated bone marrow cells. Granulocytes gated on $Gr1^{+}CD11b^{+}$, T cells gated on $CD4^{+}CD8^{+}$, immature B cells gated on $B220^{+}IgM^{low}$, mature B cells gated on $B220^{+}IgM^{high}$.

(F) Frequencies of splenic LSK cells.

(G) Gpr-HSC frequencies. Percentage of bone marrow HSC-Gpr^{pos} are represented. N = 4-7.

(H and I) Peripheral blood analysis. (H) WBC = white blood cells; (I) LY = lymphocytes.

(J) Spl/body ratio. Spl = spleen.

(K) Body weight.

(L) BM cellularity. For all panels, Control = mice in normal diet, Control recov. = mice in normal diet 8-11d after pIC injections, VitA-free = diet lacking vitamin A; VitA-free recov. = diet lacking vitamin A 8-11d after pIC injections; +/− SEM is shown. *, **, ***$p < 0.05$, 0.01 and 0.001 respectively. n.s., non-significant. N indicates biological replicates. For all experiments ≥ 2 independent experiments were performed otherwise indicated. Further details in STAR Methods.